Journal of Medicinal Chemistry

pubs.acs.org/jmc

Article

Photodynamic Therapy for *ras*-Driven Cancers: Targeting G-Quadruplex RNA Structures with Bifunctional Alkyl-Modified Porphyrins

Annalisa Ferino,[⊥] Giulia Nicoletto,[⊥] Francesca D'Este, Sonia Zorzet, Sara Lago, Sara N. Richter, Alexander Tikhomirov, Andrey Shchekotikhin, and Luigi E. Xodo*

Cite This: *J. Med. Chem.* 2020, 63, 1245−1260

Read Online

ACCESS | Metrics & More | Article Recommendations | Supporting Information

ABSTRACT: Designing small molecules able to break down G4 structures in mRNA (RG4s) offers an interesting approach to cancer therapy. Here, we have studied cationic porphyrins (CPs) bearing an alkyl chain up to 12 carbons, as they bind to RG4s while generating reactive oxygen species upon photoirradiation. Fluorescence-activated cell sorting (FACS) and confocal microscopy showed that the designed alkyl CPs strongly penetrate cell membranes, binding to *KRAS* and *NRAS* mRNAs under low-abundance cell conditions. In Panc-1 cells, alkyl CPs at nanomolar concentrations promote a dramatic down-regulation of *KRAS* and *NRAS* expression, but only if photoactivated. Alkyl CPs also reduce the metabolic activity of pancreatic cancer cells and the growth of a Panc-1 xenograft in SCID mice. Propidium iodide/annexin assays and caspase 3, caspase 7, and PARP-1 analyses show that these compounds activate apoptosis. All these data demonstrate that the designed alkyl CPs are efficient photosensitizers for the photodynamic therapy of *ras*-driven cancers.

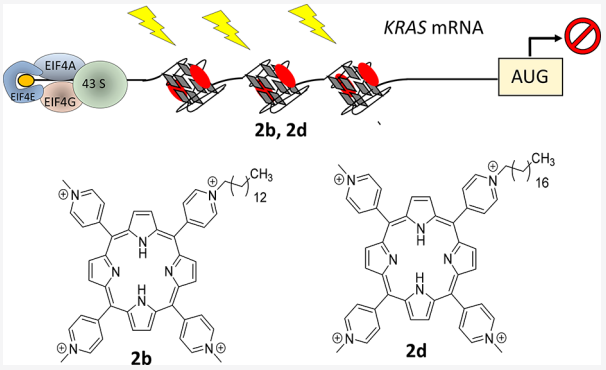

INTRODUCTION

The *ras* genes (*HRAS*, *KRAS*, and *NRAS*) are the most frequently mutated oncogene family in human cancer.[1] *Kirsten ras* (*KRAS*) is the predominant isoform, which is mutated in >95% of pancreatic ductal adenocarcinomas (PDAC), ∼50% of colorectal carcinomas, and ∼35% of lung cancers.[2] The initial step leading to a precancerous condition called "pancreatic intraepithelial neoplasia" (PanIN) is due to mutations in the *KRAS* gene.[3] When these occur in the presence of additional mutations in tumor suppressor genes (as Tp53), PanIN progresses into metastatic PDAC.[4−6] Preclinical studies based on loss of function analysis by gene expression manipulation have validated *KRAS* as an important therapeutic target for anticancer drug development.[7] This is further supported by the fact that many *ras*-driven tumors depend on the continued expression of *KRAS*.[8] Indeed, De Pinho et al.[9] have proven in an elegant study that oncogenic *KRAS* maintains pancreatic tumors through the regulation of the anabolic glucose metabolism. The dependence of the metabolic pathways on specific oncogenes has led to the concept of "oncogene addiction", according to which cancer cells although depending on a number of genetic aberrations, often develop a dependency on a particular oncogene.[10] Developing small-molecule inhibitors specific for the RAS protein is a challenging task, because the RAS protein surface lacks a suitable hydrophobic pocket to host a small molecule.[11] So, current strategies targeting proteins are (i) the association of the KRAS protein with the plasma membrane, (ii) downstream *KRAS* signaling, and (iii) *KRAS*-dependent metabolic pathways.[12−14] However, despite more than two decades of research, no anti-*ras* drugs have yet reached the clinic, thus suggesting that the *ras* genes might be "undruggable".[15−17] Given its low response to conventional chemotherapy, PDAC remains one of the human tumors with a very poor prognosis and a 5-year survival rate of only 6−7%.[18] Against this background, oncologists agree about the urgency to find alternative and innovative strategies for treating *ras*-driven genes, and this represents one of the main challenges to be addressed by medical research in the near future.

In order to propose a new anti-*KRAS* strategy, we focused on two important observations: (i) *KRAS* is characterized by a 5′-untranslated region (5′-UTR) of 193 nucleotides containing a high G content (45%), harboring several quadruplex-forming motifs able to form local G4 RNA (RG4) structures (Figure 1A); (ii) cationic porphyrins (CPs) such as tetra-*meso*-(*N*-methyl-4-pyridyl) porphine (TMPyP4) have been extensively used as G4 ligands.[19−21] G4s are unusual nucleic acid structures

Received: September 21, 2019
Published: January 13, 2020

https://dx.doi.org/10.1021/acs.jmedchem.9b01577
J. Med. Chem. 2020, 63, 1245−1260

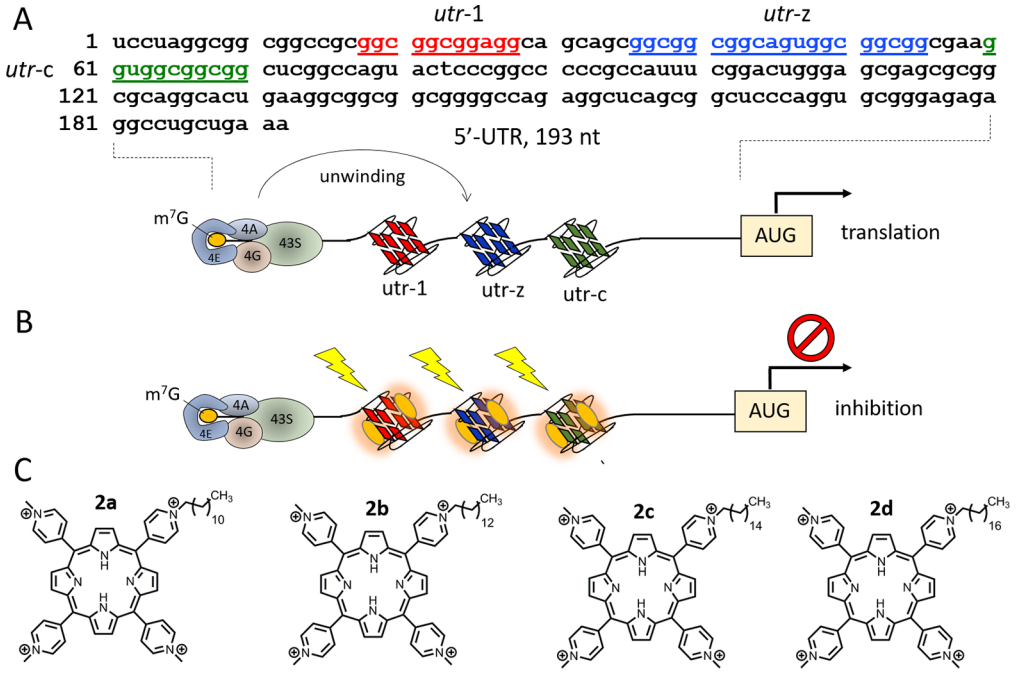

Figure 1. (A) Sequence of 193-nt 5′-UTR of the *KRAS* proto-oncogene. The sequences of the nonoverlapping G4 motifs with a G-score = 21 are shown. (B) 7-Methylguanosine (m^7G) 5′ cap is bound by proteins including EIF4A, -4E, and -4G, DEAD-box family helicases that unwind RG4 structures. 5′-UTR RG4 structures bound to porphyrins generate ROS and $^1O_2$ upon photoirradiation. (C) Structures of cationic porphyrins **2a–d** derived from TMPyP4 by replacing one methyl group with an alkyl chain of 12, 14, 16, and 18 carbons.

Scheme 1. Synthesis of Cationic 5-(4-*N*-Alkylpyridyl)-10,15,20-tri(4-*N*-methylpyridyl)-21*H*,23*H*-porphyrins 2a–d and Biotinylated Analog of 2a Biotin-NH-C_{12}-TMPyP4 (B-2a)[a]

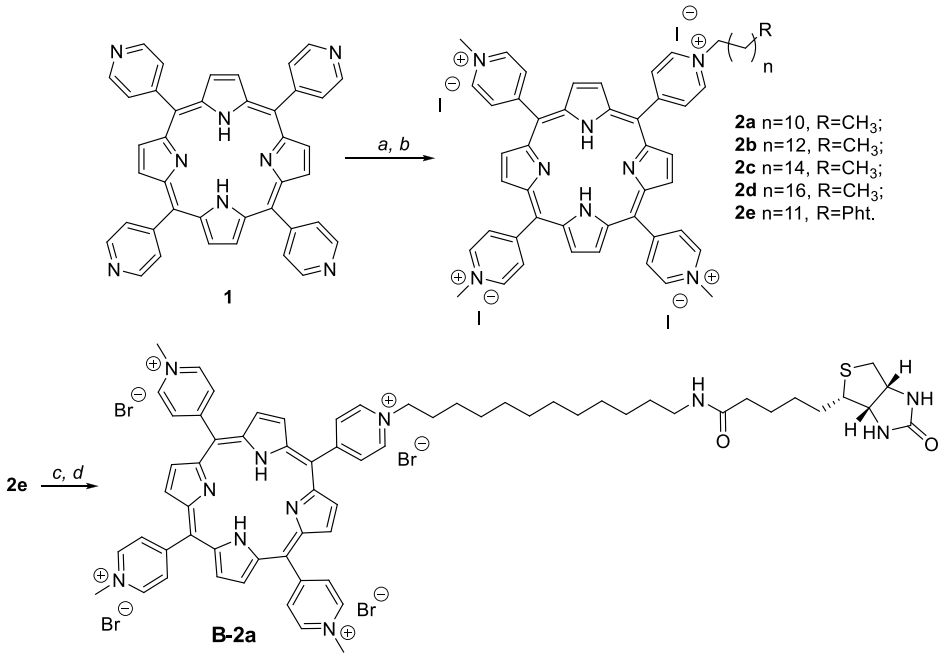

[a]Reagents and conditions: (a) iodoalkane or 2-(12-bromododecyl)phthalimide, acetic acid, argon, reflux, 72 h, then (b) iodomethane, DMF, 140 °C, 3 h, yields 23–30%; (c) hydrobromic acid, argon, boiling, 24 h, yield 80%, then (d) biotin, PyBOP, DIPEA, DMSO, rt, 1 h, yield 68%.

stabilized by the stacking upon each other of at least two G-tetrads (a planar arrangement of four guanines each forming two Hoogsteen hydrogen bonds with the neighboring bases) and by alkali metal ions (Na^+ or K^+) lying in the central cavity of the structure where they are coordinated to guanine O6.[22] Work done in the past decade strongly supports the notion that G4 DNA and RG4 are involved in gene expression regulation.[23−27] Besides binding to G4 structures, CPs have the properties of being water-soluble and generating reactive oxygen species (ROS) and singlet oxygen ($^1O_2$) upon photoirradiation.[28−30] On these premises, to target *KRAS* and *NRAS*, we propose the following approach. Single-stranded mRNA is unconstrained

https://dx.doi.org/10.1021/acs.jmedchem.9b01577
J. Med. Chem. 2020, 63, 1245−1260

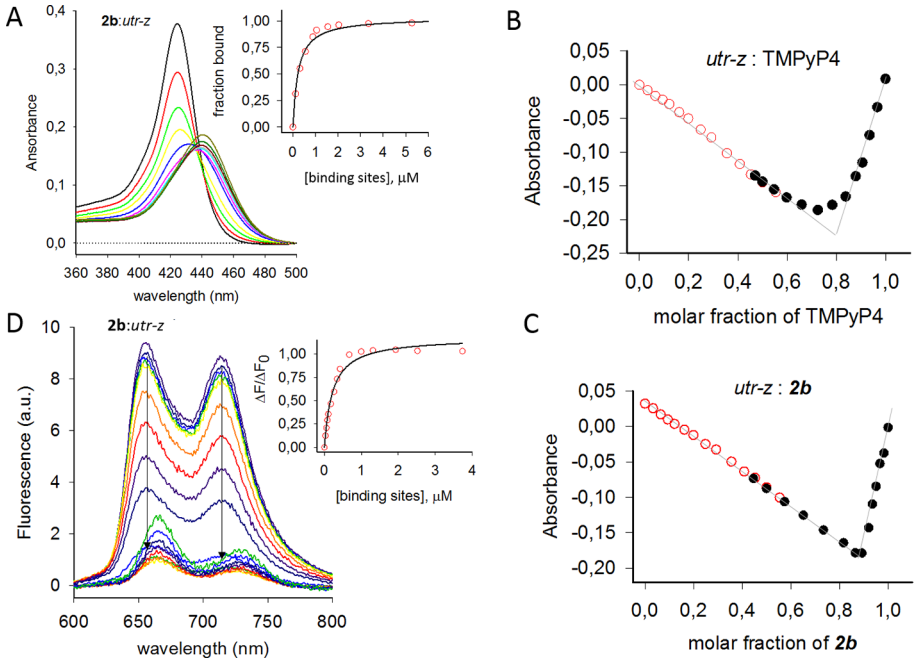

Figure 2. (A) Typical UV−vis titration of 1.6 μM **2b** in 50 mM Tris-HCl, pH 7.4, 100 mM KCl, with increasing amounts of *utr-z* RG4. The plot inside shows the best-fit of fraction of bound porphyrin versus the binding-site concentration (obtained using the Job plot stoichiometry), employing a standard two-state model. (B, C) Job plots in 50 mM Tris-HCl, pH 7.4, 100 mM KCl, relative to the binding of TMPyP4 (top panel) and **2b** (bottom panel) to *utr-z* RG4. The ordinate reports the absorbance difference at 420 nm. Plots gave stoichiometries of 4 TMPyP4 and 6 **2b** per RG4. (D) Typical fluorescence titrations of 1.0 μM **2b** with *utr-z* RG4 in 50 mM Tris-HCl, pH 7.4, 100 mM KCl. Right panel shows the fraction of bound porphyrin versus RG4 binding site concentration. The binding curve has been best-fitted with a standard binding equation (Sigma Plot 11). The K_D values obtained are reported in Table 1.

and prone to fold into secondary and tertiary structures including G4 and stem−loop elements serving as primary and secondary targets for CPs. We reasoned that in the cells CPs should preferentially bind to mRNAs with a 5′-UTR harboring G4 motifs, such as *KRAS* and *NRAS* mRNAs. Upon photoirradiation, CPs produce ROS and $^1O_2$ that mediate a photoprocess leading to the breakdown of the RG4 structures to which they are bound. This is expected to inhibit translation of the *ras* genes and activate cell death by apoptosis (Figure 1B).[31] One important aspect of this approach is that in vivo the photoprocess leading to the degradation of *KRAS* mRNA is only prompted in the irradiated tumor and not in the surrounding tissues. That is why the photodynamic strategy causes limited side effects. However, this attractive approach requires that CPs efficiently penetrate the plasma membrane and accumulate in the cytoplasm where their targets are located. To increase the uptake, we designed porphyrin derivatives of TMPyP4 with an increased level of lipophilicity. This was done by replacing one of the four methyl groups of TMPyP4 with an alkyl chain of 12, 14, 16, or 18 carbon atoms. CPs have been previously studied as photosensitizer for PDT,[28−30] but in our approach, we show for the first time that CPs target mRNA and efficiently promote apoptosis in *ras*-driven cancer cells. A critical aspect of *ras*-driven cancers is that it is not clear if the suppression of *KRAS* is compensated by the upregulation of the other *HRAS* or *NRAS* isoforms. Therefore, a pan-RAS inhibition (i.e., simultaneous inhibition of the products of the *HRAS* and *NRAS*) would be therapeutically beneficial, despite the essential role of *KRAS* for PDAC.[9] Here, we report the design and testing of CPs able to suppress *ras* genes in PDAC cells. In this article, we describe the preparation, structural characterization, and anti-*KRAS* properties of tri-*meso*-(*N*-methyl-4-pyridyl)-*meso*-(*N*-(dodecadecyl, tetradecyl, hexadecyl, or octadecyl)-4-pyridyl) porphine (**2a−d**). We focused on compounds **2b** (with an alkyl chain of 14 carbons) and **2d** (with 18 carbons), as these derivatives efficiently arrest cell growth by apoptosis. As a control, we used tetra-*meso*-(*N*-methyl-4-pyridyl) porphine (TMPyP4), as well as its regioisomer tetra-*meso*-(*N*-methyl-2-pyridyl) porphine (TMPyP2), which shows almost no affinity for RNA G4 (RG4).

RESULTS AND DISCUSSION

Synthesis of Alkyl-Modified Porphyrins (2a−d) and Biotinylated B-2a. The synthesis of a TMPyP4 derivative in which a methyl group was replaced by an alkyl chain of 12 carbons (*n*-dodecyl) has been previously reported.[32] Following the same procedure, we prepared porphyrins with trimethyl groups and an alkyl chain of 12, 14, 16, and 18 carbons. In brief, the alkylation of 5,10,15,20-tetra(4-pyridyl) porphyrin (PyP4, **1**) was carried out by a two-step procedure. Initially, PyP4 (**1**) was refluxed in the presence of 1 equivalent of the appropriate 1-iodoalkane (with 12, 14, 16, and 18 carbons) in acetic acid to yield monoalkylated porphyrins, which were then treated with 10 equivalents of iodomethane in DMF to obtain the tetra-alkylated derivatives **2a−d** (Scheme 1).

In addition, for pull-down assays, we prepared an analogue of compound **2a** bearing a biotin residue at the terminal position of the alkyl chain (**B-2a**). Porphyrin **1** was treated with 2-(12-bromododecyl)phthalimide to produce 5-(4-*N*-(12-phtalimidododecyl)pyridyl)-10,15,20-tri(4-*N*-methylpyridyl)-21*H*,23*H*-porphyrin **2e**. Cleavage of the phthalimide protecting group by refluxing with aqueous HBr for 24 h and further coupling of 12-NH_2-dodecyl end with the biotin in the presence

https://dx.doi.org/10.1021/acs.jmedchem.9b01577
J. Med. Chem. 2020, 63, 1245−1260

of PyBOP gave the biotin conjugate **B-2a** with a good yield (Figure S1, Supporting Information).

The structures of synthesized compounds were confirmed by ^{1}H and ^{13}C NMR, HRMS methods, and elemental analysis; the purity (≥95%) of final samples was estimated by HPLC (Figure S2, Supporting Information). An absence or significant broadness of the pyrrole moiety signals in the ^{13}C NMR spectra of obtained derivatives is typical for cationic porphyrins and can be explained by dynamic tautomerism.[33]

Alkyl Porphyrins Bind to 5′-UTR RNA Quadruplex (RG4) Structures. The human *KRAS* transcript contains a G-rich 5′-UTR of 193-nt harboring 33 GG runs giving rise to a multiplicity of G4 motifs (Figure 1A). By using QGRS Mapper, we identified three nonoverlapping sequences, called *utr*-1, *utr*-c, and *utr*-z, within the first 80 nt of the 5′-UTR (s-80), recognized by the G4-specific BG4 antibody.[18] These sequences display CD spectra with a strong ellipticity at 264 nm, typical of a parallel G4, that dramatically decreases in intensity with temperature.[18] UV-melting curves showed that these RG4s melt cooperatively with T_M of 53 °C (*utr*-1), 52 °C (*utr*-c), and 64 °C (*utr*-z) (uncertainty ±0.5 °C) and ΔG of G4 formation between −6.1 and −7.3 kcal/mol in 100 mM KCl.[18] Similarly, *NRAS* mRNA is characterized by a 254 nt 5′-UTR showing only a G4 motif (between −240 and −222 from ATG), forming an RG4 with 3 G-tetrads and T_M of 74 °C in 20 mM KCl (Figure S3, Supporting Information). In contrast, *HRAS* has a 5′-UTR of 94 nt containing only a G4 motif with a low propensity of folding according to QGRS Mapper. Based on these premises, in the present work we focused only on *KRAS* and *NRAS* oncogenes.

The interaction between the *KRAS* or *NRAS* RG4s and alkyl porphyrins **2b** and **2d** (and TMPyP4 as reference) was investigated by UV−vis and fluorescence titrations. Figure 2A shows a typical UV−vis titration obtained by adding increasing amounts of *KRAS utr-z* RG4 to a solution of porphyrin **2b**. Upon binding to RG4, the porphyrin induces a strong hypochromicity (~50%) and a red-shift of 13 nm of the Soret band.[34−36] Such high values of hypochromicity and red shift suggest strong stacking interactions between the porphyrin and RG4 bases.[34] We have tried to determine by UV-melting the effect of **2b** and **2d** on the stability of the RG4s, but we were unsuccessful because the alkyl porphyrins tended to aggregate at temperatures >40 °C.

The binding stoichiometry of the interaction was determined by the Continuous Variation Analysis method (Job plot).[34−36] Figure 2B,C reports typical Job plots for the interaction between *utr-z* RG4 and porphyrins TMPyP4 and **2b**. A stoichiometry of 4 porphyrins per RG4 was obtained for TMPyP4. This value is in agreement with the interaction between Pt-TMPyP4 and the G4 of the human telomere Tel22,[34] but lower than that reported for the binding of TMPyP4 with a G4 aptamer, which is 6:1.[37] In contrast, the interaction between *utr-z* RG4 and porphyrins **2b** and **2d** gave stoichiometry of 6:1 and 9:1, respectively (Figure S4, Supporting Information). These data showed that the stoichiometry depends on the length of the porphyrin alkyl chain. A similar behavior was observed with *NRAS* RG4. How can this behavior be rationalized? Sabharwal et al.[34] reported that Pt-TMPyP4 interacts with Tel22 via efficient $\pi-\pi$ stacking. These authors proposed a model, supported by light-scattering experiments, by which Pt-TMPyP4 initially stacks on the G4 ends, but in the presence of excess porphyrin, additional porphyrin molecules stack over Pt-TMPyP4 already bound to RG4 ends (aggregation). When the alkyl chain is as short as a methyl group, like in TMPyP4, only one porphyrin may aggregate on each RG4 end. This because the electrostatic repulsion between the stacked cationic porphyrins prevents further aggregation. But, when the porphyrins carry an extended alkyl chain (as **2a−d**), the forces favoring aggregation are $\pi-\pi$ end-stacking and hydrophobic interactions between the alkyl side chains. So, the longer the side chain, the stronger the hydrophobic interactions that counterbalance the repulsion between the stacked cationic porphyrins. This model rationalizes the observed stoichiometry of 9:1, 6:1, and 4:1 for **2d**, **2b**, and TMPyP4, respectively.

To determine the K_D for the interaction between porphyrins **2a−d** and RG4s, first we used a fluorescence spectroscopy method. Upon excitation at 420 nm (Soret band), the porphyrins emit between 620 and 750 nm.[36] Typical emission spectra with maxima at 650 and 715 nm are shown in Figure 2D. When a porphyrin solution is titrated with RG4, the emission is quenched, due to stacking interactions between porphyrin molecules and RG4, which favor electron transfer from the guanines to the porphyrin singlet excited state.[38] In fact, the positional TMPyP2 isomer, which is nonplanar and shows low affinity for G4 structures,[39] does not promote any quenching (Figure S5, Supporting Information). Plotting the fluorescence emission at 650 or 715 nm versus the concentration of the RG4 binding sites, we estimated K_D values by using a standard binding equation with equal and independent binding sites. As this is an oversimplification because different binding modes cannot be excluded, the K_D obtained are only estimates and not accurate values. For all the porphyrins tested K_D is <1 μM, suggesting they have a high affinity for RG4s, which increases with the length of the alkyl side chain (Table 1). We also

Table 1. K_D Values for the Interaction of RG4s with TMPyP4 and Alkyl Porphyrins 2b and 2d

	TMPyP4 K_D[a] (nM)	**2b** K_D[a] (nM)	**2d** K_D[a] (nM)
NRAS	301 ± 45	107 ± 11	32 ± 8
utr-1	454 ± 46	236 ± 23	150 ± 13
utr-c	1025 ± 281	235 ± 16	188 ± 14
utr-z	681 ± 41	219 ± 40	99 ± 7

[a]Data obtained in 50 mM Tris-HCl, pH 7.4, 100 mM KCl.

analyzed the interaction between the alkyl porphyrins and RG4 by Surface Plasmon Resonance (SPR). Due to the complex mechanism through which the alkyl porphyrins bind to RG4s (stacking and aggregation), the sensorgrams were not easy to interpret. We obtained steady-state binding curves that saturate at porphyrin concentrations <1 μM; their fit to a standard binding equation gave K_D values between 56 and 98 nM for *NRAS* RG4 and between 82 and 202 nM for *utr*-z, roughly in keeping with the fluorescence titration data (Figure S6, Supporting Information).

Besides G4 structures, TMPyP4 and alkyl derivatives bind also to duplex DNA with a comparable affinity.[40] We found by a Job plot that the binding of TMPyP4 to a 20-mer RNA stem−loop hairpin (stem−loop) exhibits a stoichiometry of 2:1, which is half of that for 20-mer *utr-z* RG4 (Figure S7, Supporting Information). This suggests that transcripts with RG4s in 5′-UTR, such as *KRAS* and *NRAS* mRNAs, have more structural elements attracting porphyrins (RG4 + stem−loops) than mRNAs with only stem−loop secondary structures. We expect that RG4-containing transcripts are more porphyrin sensitive than non-RG4 transcripts. As RG4s bind more porphyrins than stem−loop RNA, upon photoirradiation, the former produce

https://dx.doi.org/10.1021/acs.jmedchem.9b01577
J. Med. Chem. 2020, 63, 1245−1260

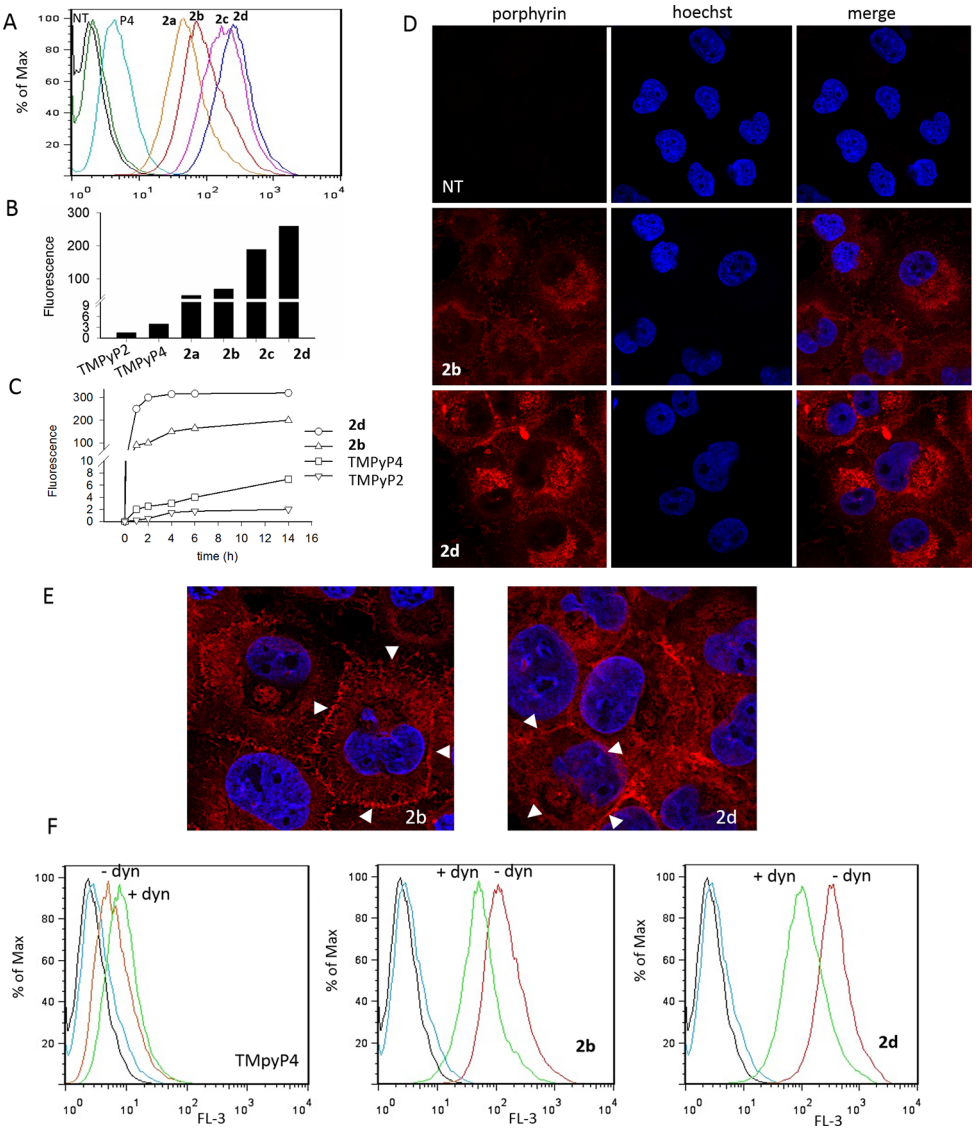

Figure 3. (A–C) FACS analyses of Panc-1 cells treated with 5 μM **2a–d**, TMPyP2, or TMPyP4 for 6 h. The histogram shows the fluorescence of the cells due to the internalization of the porphyrins. Panel C shows the uptake of 5 μM **2b**, **2d**, TMPyP2, or TMPyP4, as a function of time. (D) Confocal microscopy images of Panc-1 cells treated with 5 μM **2b** or **2d** for 6 h. The nuclei of the cells have been stained with Hoechst. Images show that the alkyl porphyrins localize in the cytoplasm. (E) Magnification of images showing that **2b** and **2d** distribute uniformly in the cytoplasm. Note the presence of CPs in the plasma membrane (white triangles sign the membrane). (F) Effect of dynasore on the uptake of TMPyP4, **2b**, and **2d**.

higher amounts of ROS and $^1O_2$ than the latter. This should make RG4 more photodegradable than stem–loop RNA.

Alkyl-Modified Porphyrins Show a Strong Uptake and Cytoplasmic Localization. The uptake by Panc-1 cells of the designed alkyl-porphyrins **2a–d** was first investigated by flow cytometry taking advantage of the red fluorescence emitted by the porphyrins excited at 480 nm (Figure 3A). The cells were treated for 6 h with 5 μM **2a–d** and analyzed by fluorescence-activated cell sorting (FACS). It can be seen that the uptake increases proportionally with the length of the alkyl side chain, that is, with the lipophilicity of the molecules: **2d** > **2c** > **2b** > **2a**. As reference, we used porphyrins TMPyP2 and TMPyP4. Nonplanar TMPyP2 shows a slight uptake, while TMPyP4 is planar and shows a higher capacity to penetrate the cell membrane. The increase of cell fluorescence as a function of the number of carbons of the alkyl chain (1, 12, 14, 16, and 18) are reported in a histogram (Figure 3B), which shows that the uptake increases up to 2 orders of magnitude as the alkyl chain increases from 1 (TMPyP4) to 18 (**2d**) carbons. We also analyzed the uptake of **2b**, **2d**, TMPyP2, and TMPyP4 as a function of time. The results reported in Figure 3C show that the porphyrins with an alkyl chain of 14 or 18 carbons rapidly internalize in the cells (in ~2 h), whereas TMPyP2 and TMPyP4 penetrate the cells with a much slower kinetics. After 16 h of incubation, the amounts of internalized **2b** and **2d** are, respectively, 24- and 38-fold higher than that of TMPyP4, while the internalization of TMPyP2 is about 2–3-fold lower than that of TMPyP4. These data prove that adding a lipophilic chain to TMPyP4 has a dramatic effect on uptake, which increases proportionally with the length of the alkyl chain.

Next, we performed confocal microscopy experiments in order to examine the intracellular localization of the designed alkyl porphyrins. Figure 3D shows Panc-1 cells treated with Hoechst, a dye that stains the cell nucleus (top panel). The intracellular distribution of **2b** and **2d** was detected by porphyrin excitation at 470 nm. Confocal sections of the cells treated with

https://dx.doi.org/10.1021/acs.jmedchem.9b01577
J. Med. Chem. 2020, 63, 1245–1260

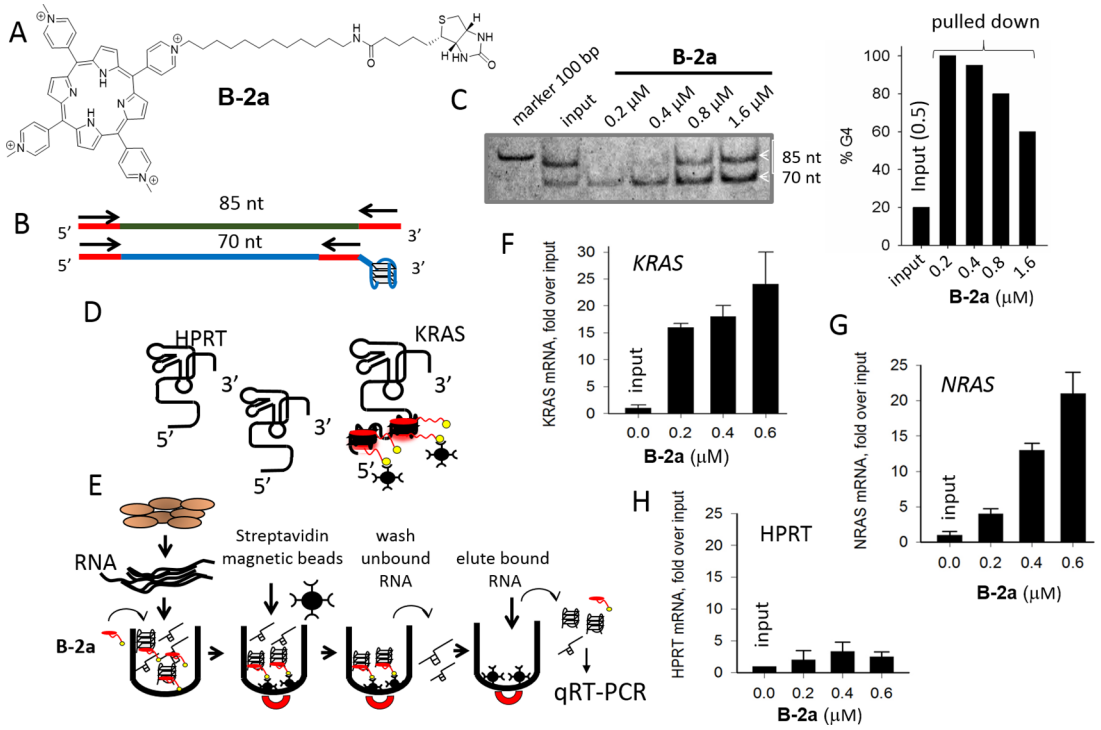

Figure 4. (A) Structure of ligand **B-2a**; (B) Design of the pull down assay to test the capacity of ligand **B-2a** to pull down G4 from a DNA mixture; (C) PAGE showing the separation of the amplified DNA fragments of 70 and 85 nt, obtained from a DNA mixture at r = 0.5. Histogram reporting the percentage of G4 in the pulldown DNA and in the input; (D) Total cellular mRNAs contain *KRAS* and *NRAS* mRNAs with RG4 structures in 5′-UTR. RG4s interact with ligand **B-2a**. *HPRT* and *β2-microglobulin* do not interact or only slightly interact with ligand **B-2a**; (E) The streptavidin−biotin pull-down assay: **B-2a** pulls down preferentially mRNAs with RG4s. The recovered mRNA was used to determine by RT-qPCR the amounts of *KRAS*, *NRAS*, *β2-microglobulin* and *HPRT* mRNAs; (F, G) The histograms show the ratio of *KRAS* and *NRAS* over *HPRT* mRNAs in the input (total RNA extract, fixed to 1) and in recovered RNA from pulldowns with increasing amounts of **B-2a**. An enrichment of both *KRAS* and *NRAS* mRNAs over *HPRT* of about 25-fold was obtained with both transcripts, suggesting that the biotinylated ligands bind to *KRAS* and *NRAS* mRNAs present in the total cellular extract; (H) No enrichment of *HPRT* over *β2-microglobulin* (or vice versa) was observed.

2b (middle panel) or **2d** (bottom panel) evidenced that the fluorescence was localized in the cytoplasm. Figure 3E shows a magnification of Panc-1 cells treated with **2b** and **2d**. The alkyl porphyrins appear uniformly distributed in the cytoplasm, as expected from ligands designed to target mRNA. To get an insight into the uptake mechanism, we used dynasore, a noncompetitive inhibitor of the dynamin GTPase activity that blocks dynamin-dependent endocytosis in cells.[41] Figure 3F shows that dynasore reduces the uptake of **2b** and **2d** but not of TMPyP4, suggesting that the transport of the alkyl porphyrins **2a−d** in the cells is mediated by endocytosis. This explains why **2a−d** are taken up by the cells more efficiently than TMPyP4. The fact that the porphyrins clearly delimit the cell surface suggests that they diffuse into the lipid bilayer and most likely penetrate the cell membrane also by passive diffusion. This is supported by the finding that in Panc-1 cells the uptake at 4 °C is 24% the uptake at 37 °C with **2b** and 47% with **2d**. A similar behavior was observed with murine NIH 3T3 and human HEK 293 cells (Figure S8, Supporting Information).

Alkyl-Modified Porphyrins Bind to *KRAS* and *NRAS* Transcripts Within the Transcriptome. Having found that the alkyl porphyrins accumulate in the cytoplasm, we asked if these porphyrins are able to recognize within the transcriptome the RG4 structures in *KRAS* and *NRAS* mRNAs under low-abundance cellular conditions. To this purpose, we set up a biotin−streptavidin pull-down assay by using porphyrin **2a** conjugated to biotin (ligand **B-2a**, Figure 4A). First, we checked if ligand **B-2a** was able to form a sufficiently stable complex with a G4 structure that can be pulled down through its biotin moiety by streptavidin coated beads. To this purpose, we designed two DNA strands of 95 and 89 nt, the former of which contained a G4 motif at the 3′ end (telomeric *htel*). Both strands had identical sequences at the 5′ and 3′ ends, so that two DNA fragments of 70 and 89 nt could be amplified with the same couple of primers (Figure 4B). We prepared four DNA mixtures of the two strands in 50 mM Tris-HCl, pH 7.4, 50 mM KCl (KCl buffer). The total strand concentration of each mixture was 0.2 μM, but the ratio (r) between the two strands, r = [95-nt]/[89-nt], was fixed at 0.25, 0.5, 1.0, and 2.0. In KCl buffer, the G4 motif in the 95-nt strand formed a stable antiparallel G4 structure with a T_M of 63 °C (Figure S9, Supporting Information).[42] The DNA mixtures were incubated for 1 h with increasing amounts of biotinylated ligand **B-2a** (0.2, 0.4, 0.8, and 1.6 μM). The DNA captured by ligand **B-2a** was pulled down with streptavidin-coated magnetic beads and recovered with 0.8 M NaCl. Input (untreated) and recovered DNA were amplified and the 70 and 85 nt products were separated by 12% PAGE and quantified. The % G4 strand in the input and pulled down mixtures was determined. A typical result is shown in Figure 4C. PAGE shows that when the input was fixed at r = 0.5 (G4-strand/ss strand = 1/2), the DNA pulled down by 0.2 and 0.4 μM ligand **B-2a** contained only the G4 strand (95 nt strand), suggesting that ligand **B-2a** bound tightly to the G4 structure (see histogram): a property necessary for the next step of the experiment. Note that when ligand **B-2a** was used at

https://dx.doi.org/10.1021/acs.jmedchem.9b01577
J. Med. Chem. 2020, 63, 1245−1260

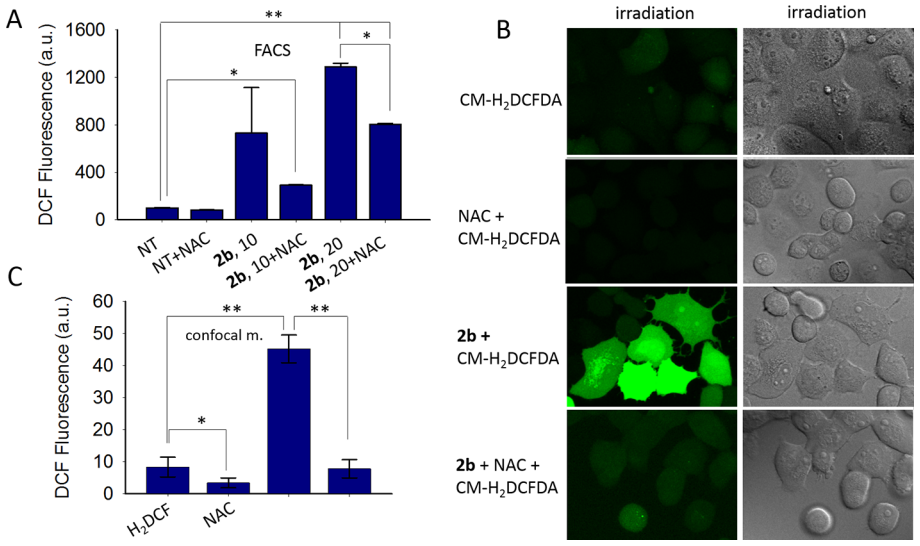

Figure 5. (A) Production of ROS in Panc-1 cells by alkyl porphyrin **2b**. The cells have been treated with CM-H_2DCFDA and **2b** in the presence or absence of 5 mM NAC, photoirradiated (7.2 J/cm^2), and analyzed by FACS. The green fluorescence generated by photoactivated **2b** in Panc-1 cells is proportional to the ROS produced. The amount of fluorescence has been measured and reported in a histogram. (B, C) Cells treated as in panel A except that the fluorescence emitted by the cells is detected by confocal microscopy. Left panels show the emission of oxidized CM-H_2DCFDA. Right panels show DIC images of the cells. For simplicity CM-H_2DCFDA was written as H_2DCF. Student's *t*-test: $^*P < 0.05$; $^{**}P < 0.01$.

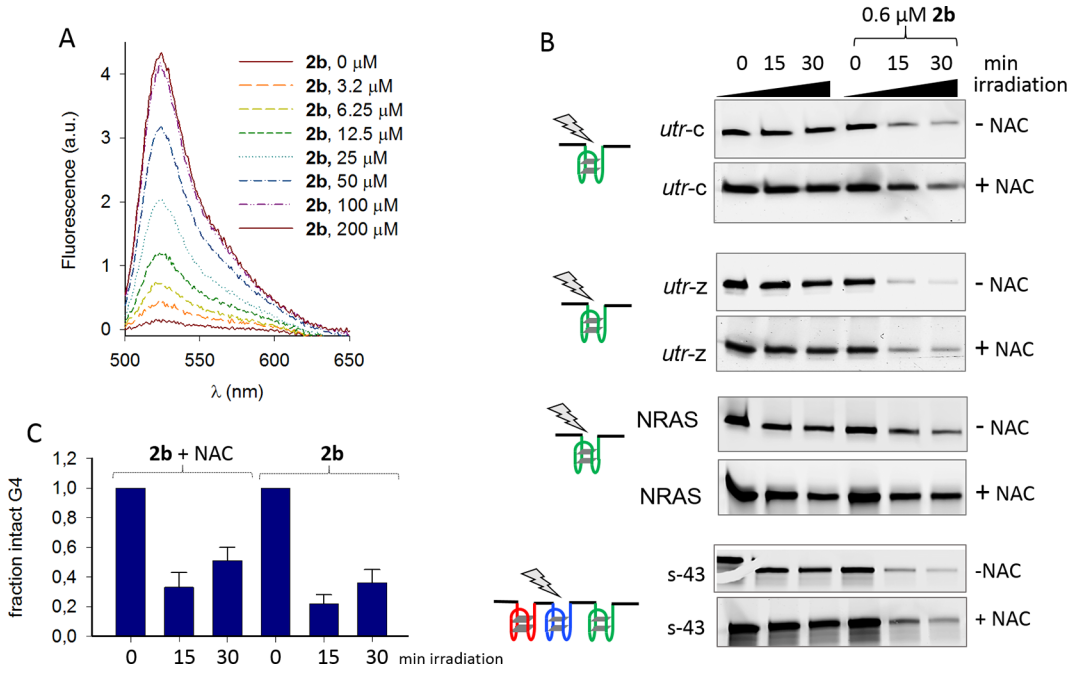

Figure 6. (A) Production of ROS by a solution of **2b** and CM-H_2DCFDA in a test tube, after photoirradiation. The increase of fluorescence as a function of **2b** concentration, due to oxidation of 5 μM CM-H_2DCFDA into CM-DCFDA, is proportional to ROS. (B) ROS produced by photoactivated alkyl porphyrin **2b** break down the *ras* RG4s. The PAGE analysis shows the residual RG4 as a function of increasing irradiation times. (C) Histogram showing the average of all RG4 residuals after 15 and 30 min irradiation in the presence of **2b**. Note that when **2b** was added to the mixture with NAC (10 mM), the residual RG4 increased, as expected.

concentrations >0.4 μM, the pulled down sample contained also some ssDNA.

Next, pull-down experiments were performed by replacing the DNA mixtures with total RNA extracted from Panc-1 cells. Cellular RNA is composed of ribosomal, transfer, and, in minimal part, mRNA. As schematized in Figure 4D, the transcriptome is composed by mRNAs without RG4s (as *HPRT* and *β2-microglobulin*) and mRNAs with 5′-UTRs having RG4s such as those of *KRAS* and *NRAS*. Therefore, the transcripts may have for the alkyl porphyrins only stem−loop binding sites or stem−loop and RG4 binding sites. Based on this assumption, total RNA extracted from Panc-1 cells was incubated with ligand **B-2a** and the captured RNA was pulled down with streptavidin-coated magnetic beads (Figure 4D,E). The amounts of *KRAS*, *β2-microglobulin*, and *HPRT* transcripts in the recovered RNA were determined by qRT-PCR and compared with the corresponding amounts in the input (untreated cellular RNA). The results showed that *KRAS*

https://dx.doi.org/10.1021/acs.jmedchem.9b01577
J. Med. Chem. 2020, 63, 1245−1260

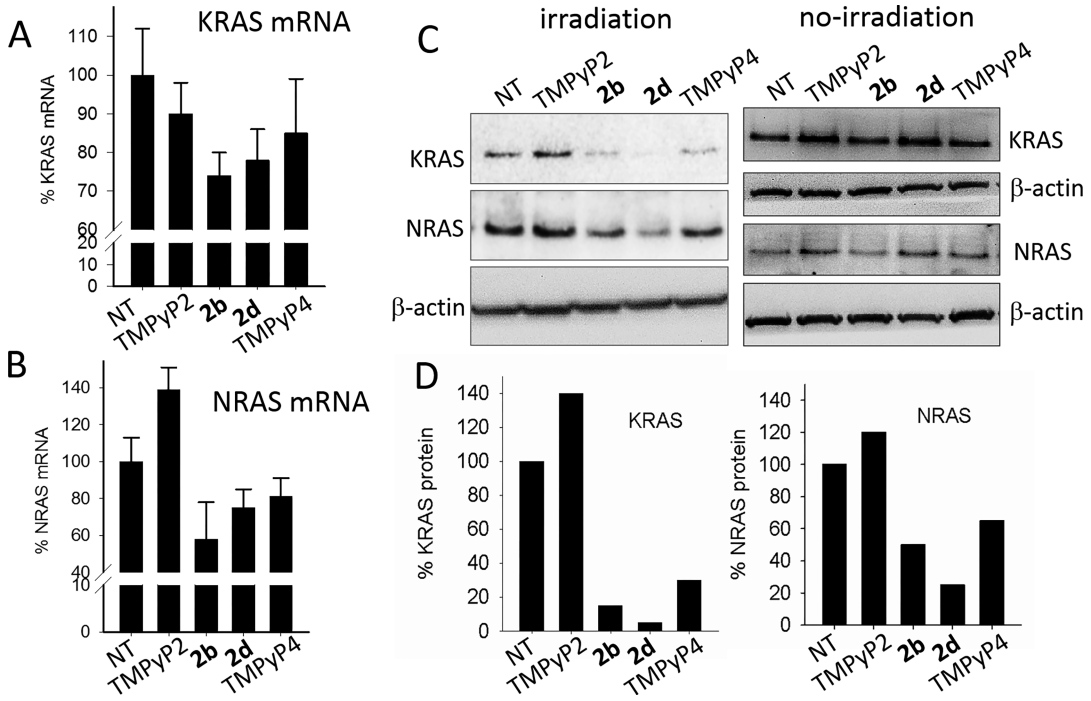

Figure 7. (A,B) Quantitative RT-PCR determination of *KRAS* and *NRAS* transcripts in pancreatic Panc-1 cells treated with 15 nM TMPyP2, TMPyP4, **2b**, and **2d** and photoirradiated; (C) Western blots showing the levels of KRAS and NRAS proteins in Panc-1 cells treated with 15 nM TMPyP2, TMPyP4, **2b**, and **2d** and photoirradiated (left panels) or in the dark (right panels); (D) Histogram showing the level of proteins KRAS and NRAS with respect to *β*-actin in Panc-1 cells after photoirradiation.

mRNA compared to *HPRT* and *β2-microglobulin* mRNAs increased up to 25-fold, in a way proportional to the concentration of ligand **B-2a** (0.2 to 0.6 μM), suggesting that the alkyl porphyrin **B-2a** binds to the *KRAS* mRNA present in the whole transcriptome (Figure 4F). A similar result was observed with *NRAS* mRNA (Figure 4G). As a control we measured, in the recovered RNA obtained at various **B-2a** concentrations, *HPRT* compared to *β2-microglobulin*, and expectedly no significant enrichment was observed (Figure 4H) (similarly, no enrichment of *β2-microglobulin* over *HPRT* was observed). Together, the data demonstrate that the designed alkyl porphyrins bind efficiently to the *ras* mRNAs present in the whole transcriptome under low abundance cellular conditions.

Photoactivated Alkyl-Modified Porphyrins Generate ROS that Break Down RG4s. The therapeutic approach that we propose is based on the assumption that the designed alkyl porphyrins efficiently generate ROS in the cells upon photoirradiation. To prove this in Panc-1 cells, we used chloromethyl-2′,7′-dichlorodihydrofluorescein diacetate (CM-H_2DCFDA), which is cleaved by intracellular esterases and transformed into CM-H_2DCF. This dye becomes highly fluorescent when it is oxidized to CM-DCF by intracellular ROS.[43] When Panc-1 cells are cotreated with alkyl porphyrin **2b** and CM-H_2DCFDA, they emit green fluorescence upon photoirradiation, due to the production of ROS by the activated porphyrin. The cellular emission can be measured by FACS. In the presence of *N*-acetylcysteine (NAC), an antioxidant sulfhydryl substance that behaves as a ROS scavenger,[44] CM-H_2DCF should not be oxidized and the fluorescence of the cells should be significantly reduced. Figure 5A shows the fluorescence measured by FACS of Panc-1 cells treated with 10 and 20 nM **2b** and 10 μM CM-H_2DCFDA in the presence or absence of 5 mM NAC. It can be seen that **2b** upon photoirradiation generates ROS in a dose-dependent manner. ROS are significantly reduced when the cells are also treated with NAC, suggesting that the increase of cell fluorescence is indeed due to intracellular production of ROS by the porphyrin. This photoprocess was also followed by confocal microscopy (Figure 5B). Panc-1 cells treated with CM-H_2DCFDA in the absence or presence of NAC did not emit green fluorescence following photoirradiation. When they are cotreated with CM-H_2DCFDA and porphyrin **2b**, they showed a strong emission in the green due to the oxidation of CM-H_2DCF by the ROS generated by **2b**. So, the intensity of the green fluorescence emitted by the cells is directly proportional to ROS production. Expectedly, when the cells were treated with **2b** in the presence of CM-H_2DCFDA and NAC, the fluorescence was dramatically lower, due to the ROS scavenger effect of NAC. We measured the intensity of the green fluorescence from representative fields (n = 5) and reported the data in a histogram (Figure 5C): the results are in agreement with those obtained by FACS. We can therefore conclude that upon photoirradiation the designed alkyl porphyrins generate ROS in the cells.

Next, we asked if the photoactivated alkyl porphyrins bound to RG4 were able to break down RNA structures. Figure 6A shows that CM-H_2DCFDA is oxidized by **2b** also in the test tube: the photoirradiation of a solution containing CM-H_2DCFDA and increasing amounts of **2b** emits fluorescence in a dose−response manner. We then exposed the RG4 sequences labeled with Cy5.5 to 0.6 μM porphyrin **2b** and analyzed the samples by electrophoresis after 15 and 30 min of irradiation. Figure 6B shows that when the oligoribonucleotides are irradiated in the absence of porphyrin, they are not degraded. In contrast, in the presence of 0.6 μM **2b**, photoirradiation causes the breakdown of the RG4 structures. As expected for a process mediated by ROS, NAC reduces the degradation of RG4s. We reported in a histogram the average of all RG4

https://dx.doi.org/10.1021/acs.jmedchem.9b01577
J. Med. Chem. 2020, 63, 1245−1260

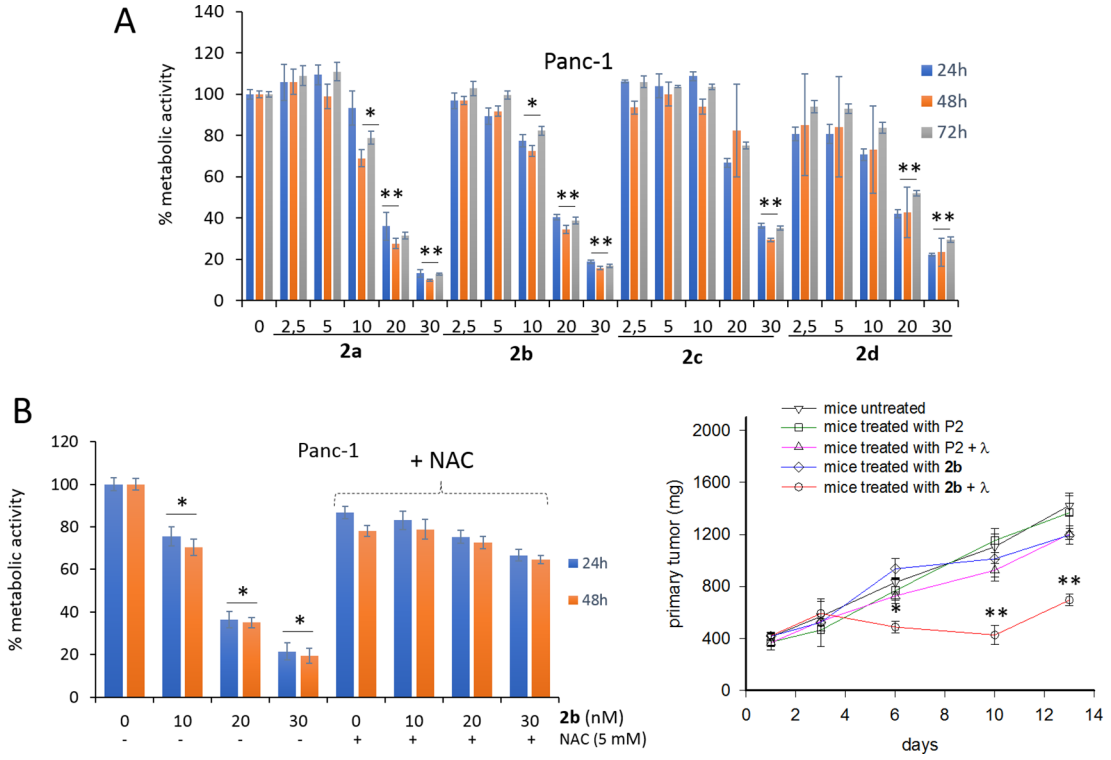

Figure 8. (A) Metabolic activity (%) of Panc-1 cells treated with alkyl porphyrins **2a**–**d** at 24, 48, and 72 h after photoirradiation. (B) Effect of NAC (5 mM) on the metabolic activity of Panc-1 cells treated with **2b** at 24 and 48 h after photoirradiation. Student's *t*-test: $^{**}P < 0.01$. (C) Effect of **2b** (3 mg/kg) and TMPyP2 (30 mg/kg) on the growth of a Panc-1 xenograft in SCID mice after photoirradiation with a diode laser at 660 ± 5 nm (fluence 193 J/cm^2). Statistical analysis by ANOVA: $^{*}P < 0.05$; $^{**}P < 0.01$.

residuals detected after 15 and 30 min photoirradiation in the presence of **2b**. The data indicate that the photodynamic process strongly degrades the RG4s, with an RG4 residual of ∼30% of the control (untreated cells). In the presence of NAC, residual RG4 increased up to ∼50% (Figure 6C). We also tested the ability of **2b** to break down upon photoirradiation *utr-z* and *utr-c* in duplex and a stem–loop hairpin. We found that **2b** had a significantly lower effect on the duplexes and hairpin than on RG4s (Figure S10, Supporting Information). These results show that the photoactivated alkyl porphyrins break down RG4 structures more efficiently than duplex RNA. This can be rationalized as follows. An alkyl porphyrin stacked on an external G-tetrad of RG4 is in contact with 4 guanines, while intercalated in double-stranded RNA, it makes contacts with only 2 nucleobases. This means that RG4 is more susceptible of cleavage mediated by ROS than duplex RNA. In addition, as several porphyrin molecules aggregate on the external G-tetrads of RG4, they produce by photoirradiation high amounts of $^1O_2$ and ROS that efficiently cleave RNA. In the light of these results we investigated if the alkyl porphyrins **2b** and **2d**, which both show efficient uptake, were able to break down the *ras* transcripts in Panc-1 cells. We selected porphyrin **2b**, because it contains a shorter alkyl chain and shows a lower tendency to aggregate, and porphyrin **2d**, which is more lipophilic, due to its longer alkyl chain, less prone to aggregation, and probably more inclined to associate with the membranes.

Alkyl-Modified Porphyrins Inhibit *KRAS* and *NRAS* Expression upon Photoactivation. The levels of cellular *KRAS* and *NRAS* mRNAs after photoirradiation have been measured by quantitative RT-PCR. Figure 7A,B shows the amounts of *KRAS* and *NRAS* transcripts detected 4 h after photoirradiation (7.2 J/cm^2) of the cells. It can be seen that both alkyl porphyrins **2b** and **2d**, at a concentration as low as 15 nM, decrease the levels of *KRAS* and *NRAS* transcripts. We also measured by Western blot the levels of KRAS and NRAS proteins in the treated cells observing that **2b** and **2d** dramatically reduced the amount of protein expressed: KRAS protein to ∼20% and 5% of the control, respectively, and NRAS protein to ∼50% and 25% of the control (Figure 7C,D). The reason why the KRAS protein was more suppressed than the corresponding transcript is most likely due to the fact that the alkyl porphyrin causes basically the photocleavage of the 5′-UTR region. So, the amplification of a downstream region in *KRAS* mRNA would also detect transcripts with a degraded or partially degraded 5′-UTR that cannot be translated (we could not efficiently amplify the 5′-UTR region because of its high G content). Moreover, on binding to the 5′-UTR region, the alkyl porphyrins may also suppress translation either by inhibiting the assembly of the preinitiation complex at the 5′ m^{7}G cap of the transcript or by disturbing the scanning of the preinitiation complex toward AUG.[26,27,45,46] Note that when the cells are not photoirradiated, the porphyrins at nanomolar concentrations have little or no effects on *KRAS* and *NRAS* expression (Figure 7C).

Effect of Alkyl Porphyrins on Metabolic Activity and Panc-1 Xenograft in Mice. Mutant *KRAS* is an oncogene that plays a critical role in maintaining a high metabolic rate in cancer cells. DePihno and co-workers have demonstrated that *KRAS* reprograms both glucose and glutamine metabolism in order to generate the biomass and the reducing power necessary to feed a high proliferation rate.[9] We tested the impact of the designed alkyl porphyrins on the metabolic activity in Panc-1 and MIA PaCa-2 pancreatic cancer cells by a resazurin assay using a dye that becomes fluorescent in metabolically active cells as it is

https://dx.doi.org/10.1021/acs.jmedchem.9b01577
J. Med. Chem. 2020, 63, 1245−1260

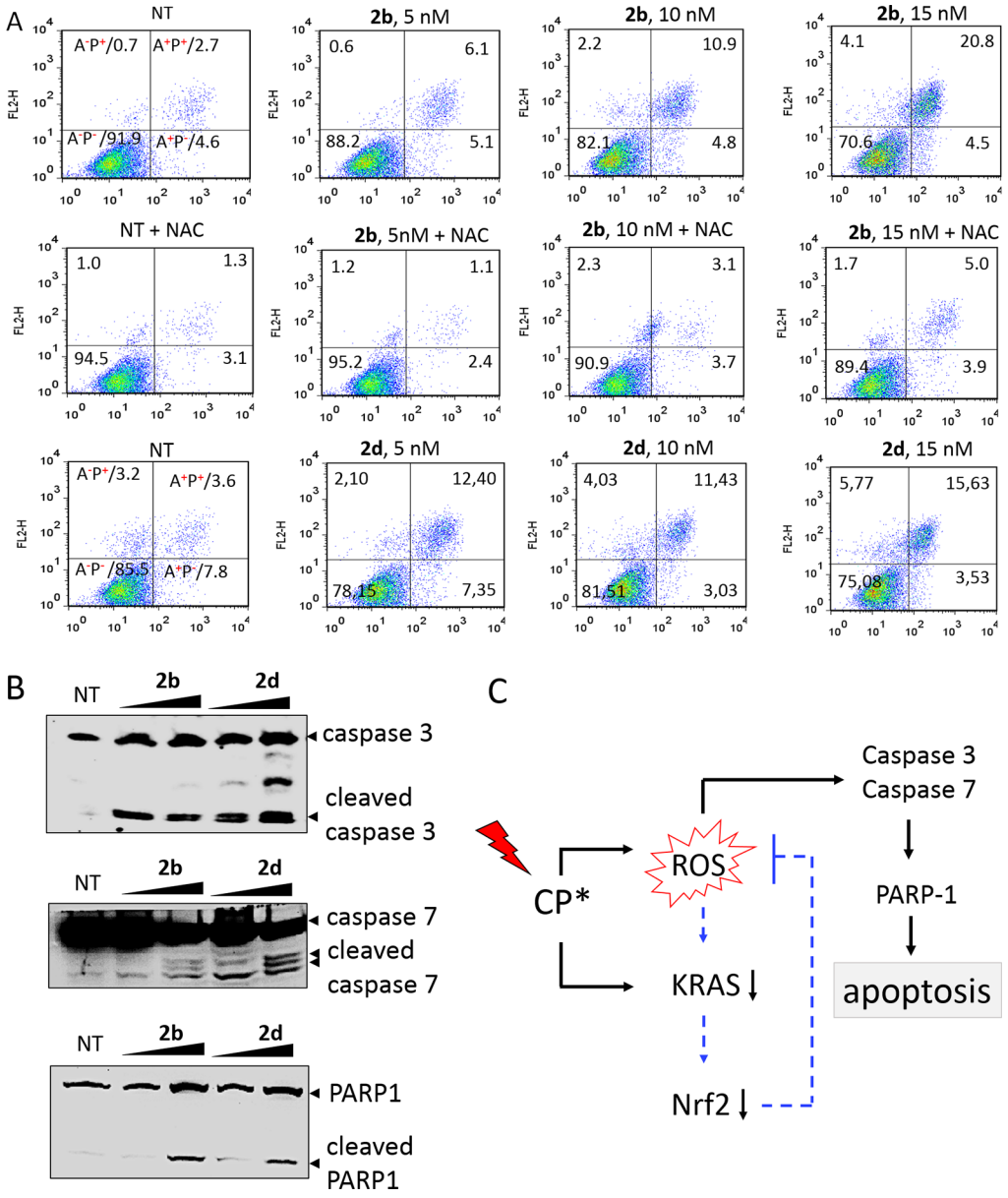

Figure 9. (A) Annexin−propidium iodide experiment with Panc-1 photoirradiated with increasing amounts of **2b** (5, 10, and 15 nM) in the presence and absence of NAC (5 mM) and **2d** (5, 10, and 15 nM). (B) Western blot showing the cleavage of caspases 3 and 7 in Panc-1 cells photoirradiated with **2b** and **2d**. Cleavage of PARP-1 observed after photoirradiation of the cells. (C) Mechanism for the activation of apoptosis by cationic porphyrins.

reduced by NADH. Figure 8A shows that the metabolic activity in Panc-1 cells strongly drops between 24 and 72 h following photoirradiation. The inhibitory effect is quite strong, as the EC_{50} value at 48 h is 13.1 ± 1.4 nM for **2a**, 13.7 ± 0.7 nM for **2b**, 19.2 ± 3.5 nM for **2c**, and 16.4 ± 2.1 nM for **2d**. A similar result was obtained with MIA PaCa-2 pancreatic cancer cells harboring the G12C point mutation, while in noncancerous HEK 293 cells, the alkyl porphyrins showed a weaker activity (Figure S11, Supporting Information). To check if the observed inhibitory effect of the metabolic activity is actually triggered by the ROS generated by the photoactivated alkyl porphyrins, we performed two experiments. First, in the dark, the designed alkyl porphyrins did not show any impact on the metabolic activity at concentrations as low as 20 nM (Figure S12, Supporting Information), second, the metabolic activity in Panc-1 cells cotreated with alkyl CPs and NAC was strongly reduced (Figure 8B). Finally, we tested the activity of **2b** and TMPyP2 as a control in SCID mice in which we implanted a subcutaneous Panc-1 tumor xenograft. SCID mice with a Panc-1 tumor xenograft of ∼30−50 mm^3 were randomized into five groups: group 1 (n = 4) untreated mice; groups 2 and 3 (n= 4) mice intratumorally injected with 50 μL solution containing TMPyP2 (30 mg/kg) and **2b** (3 mg/kg), respectively; groups 4 and 5 (n= 3) mice intratumorally injected with TMPyP2 (30 mg/kg) and **2b** (3 mg/kg) and after 2 h the xenograft was photoirradiated with a diode laser at 660 ± 5 nm (fluence of 193 J/cm^2, irradiation of the Q-1 band of the porphyrin), in the optical therapeutic window where light is harmless and shows its maximum depth of tissue penetration. Although the number of mice in each group was not high, the results clearly showed that porphyrin **2b** strongly retarded the growth of the tumor xenograft. The treatment with TMPyP2 and **2b** without irradiation did not arrest the tumor growth compared to the control (untreated group). In contrast, when the xenograft was

https://dx.doi.org/10.1021/acs.jmedchem.9b01577
J. Med. Chem. 2020, 63, 1245−1260

photoirradiated, a significant delay in tumor growth was obtained with **2b** but not with TMPyP2, starting from day 6 ($P < 0.01$ by ANOVA). At days 10 and 13, the inhibitory effect of **2b** on tumor growth was even more evident ($P < 0.001$ by ANOVA) (Figure 8C). The lack of activity shown by TMPyP2 was expected as this porphyrin shows no affinity for RG4. Additionally, the presence of **2b** in the tissues surrounding the irradiated tumor cannot promote any off-target effects simply because a nonexcited porphyrin does not produce ROS. The mechanism by which **2b** reduces tumor growth will be discussed in the next section.

Suppression of *ras* Genes by Photoactivated Alkyl Porphyrins Induces Apoptosis. Previous studies from our laboratory showed that pancreatic cancer cells respond to the suppression of *KRAS* by activating apoptosis.[31] We tested by annexin V−propidium iodide if the designed alkyl porphyrins reduce cell growth by apoptosis. Figure 9A shows the effect of **2b** on Panc-1 cells in the presence and absence of NAC. The majority of untreated cells are viable and nonapoptotic (~92%, annexin V^-/PI^-, for simplicity A^-P^-). NAC does not have any effect on untreated cells (not shown). When the cells are treated with 5, 10, and 15 nM **2b** and photoirradiated, there is an increase of apoptotic A^+P^- (early apoptotic) and A^+P^+ (late apoptotic) populations up to 20%. This heterogeneity of apoptotic cells might be explained on the grounds that they undergo apoptosis in a nonsynchronized fashion. Note that NAC strongly reduced both A^+P^- and A^+P^+ cells, as expected for a process mediated by ROS. A similar result was obtained with alkyl porphyrin **2d**, which increased A^+P^- and A^+P^+ apoptotic populations up to 25%. As a next step, we analyzed apoptosis by Western blots (Figure 9B). An important signaling cascade occurring in apoptosis is the activation of caspases, which are normally present in the cells in an inactive form. Executioner caspases 3 and 7 are activated by cleavage. In the active form, they initiate apoptosis by cleavage of key proteins of the cell, such as PARP1. Cleavage and inactivation of PARP1 by caspases are indeed considered hallmarks for apoptosis.[47] Figure 9B shows that photoactivated **2b** and **2d** induced the cleavage of the caspases 3/7 and PARP1, which is present in the cells as intact (115 kDa) and cleaved (85 kDa) protein. These data clearly demonstrate that alkyl porphyrins induce apoptosis in pancreatic cancer cells. In Figure 9C, we report a possible mechanism for the activation of apoptosis. Under normal metabolic conditions, the *KRAS* oncogene stimulates the expression of Nrf2, the redox sensor of the cells that activates the detoxification enzymes, thus bringing down intracellular ROS and favoring cell growth.[48−51] But when the ROS level is high, as occurs when the cells are treated with porphyrins and irradiated, the expression of *KRAS* is inhibited, and thus Nrf2 is not activated. Under these conditions, the detoxification program is not activated. High ROS activate executioner caspases 3 and 7, which induce cell death by damaging vital proteins such as PARP-1.

CONCLUSION

PDAC is a human malignancy resistant to conventional chemotherapies.[52] Identification of novel molecular therapies is therefore urgently needed. Recent studies suggest that the most promising strategy for the treatment of PDAC should be a targeted therapy against *KRAS*, because of its key role in controlling the PDAC metabolism.[9] In our study, we have designed and tested the capacity of alkyl porphyrins to reduce the growth of pancreatic cancer cells in cultured cells, as well as in a xenograft. Our study shows that the designed alkyl porphyrins (i) bind to RG4s in *ras* transcripts causing their breakdown upon photoirradiation, (ii) efficiently internalize in the cytoplasm of pancreatic cancer cells by endocytosis and passive diffusion, (iii) produce ROS in pancreatic cancer cells upon photoirradiation, and (iv) strongly reduce the metabolic activity in Panc-1 cells with IC_{50} in the range of 15−30 nM. Compound **2b** also reduces cell growth of a Panc-1 xenograft and (v) induces apoptosis as indicated by annexin/propidium iodide assay, activation of executioner caspases 3 and 7, and cleavage of PARP-1.

Our data identify alkyl porphyrins as particularly attractive anticancer drugs for *ras*-driven cancers, as they cause the suppression of the *ras* oncogenes at nanomolar concentrations. Another important point is the following: a bioinformatic analysis performed on the human UTR full collection yielded that 8% of the 5′-UTR contained at least one RG4.[46] One might therefore argue that alkyl porphyrins not only bind to the *ras* transcripts but also to other transcripts. This is true, but the alkyl porphyrins are photoactivated only in the irradiated tumor and not in the surrounding tissues. Additionally, as pancreatic cancer cells are addicted to *KRAS*, its suppression will have stronger effect than the suppression of other genes. Alkyl porphyrins are used in the nanomolar concentration range, where the non-irradiated alkyl porphyrins do not have any effect on the metabolism of the cells. That is why this strategy is particularly attractive for cancer therapy. Recently, Sugimoto and co-workers[53] reported that the expression of *NRAS* can be broken down photodynamically by phthalocyanines. The fact that these compounds are used at concentrations nearly 3 orders of magnitude higher than the concentrations used for the designed alkyl porphyrins suggests the great impact of the alkyl chain on the bioactivity of these small molecules. Small molecules at nanomolar concentrations are likely to elicit lower off-target effects than when they are used at micromolar concentrations. In fact, our alkyl porphyrins at nanomolar concentrations are not toxic, as indicated by lack of effects on protein level and metabolic activity.

Finally, many human tumors frequently show addiction to mutated RAS proteins. These tumors are strongly dependent on the *ras* genes, so the use of small molecules that simultaneously inhibit *KRAS* and *NRAS* would be therapeutically beneficial.

EXPERIMENTAL SECTION

General Information. NMR spectra were recorded either on Varian Mercury 400 Plus instrument operating at 400 MHz (^{1}H NMR) and 100 MHz (^{13}C NMR) or Bruker AVANCE III 500 (Bruker Biospin, Germany) NMR spectrometer equipped with a broadband Z-gradient probe head with direct observe BB coil (PABBO) at 500.18 MHz for ^{1}H and 125.77 MHz for ^{13}C. Chemical shifts were measured in DMSO-d_6 using tetramethylsilane as internal standard. Analytical TLC was performed on Silica Gel F_{254} plates (Merck, Germany) and column chromatography on Silica Gel Merck 60. Melting points were determined on a Buchi SMP-20 apparatus and are uncorrected. High-resolution mass spectra were recorded with electron-spray ionization on a Bruker Daltonics micro-OTOF-QII instrument. UV spectra were recorded on a Hitachi-U2000 spectrophotometer. All solutions were evaporated at reduced pressure on a Buchi-R200 rotary evaporator at a temperature below 45 °C. All products were vacuum-dried at room temperature. All solvents, chemicals, and reagents were obtained commercially and used without purifications. TMPyP4 and TMPyP2 have been purchased from Porphyrins Systems (Lubeck, Germany). The purity of final compounds **2a−d** and **B-2a** was >95% as determined by HPLC analysis (Figure S2, Supporting Information).

https://dx.doi.org/10.1021/acs.jmedchem.9b01577
J. Med. Chem. 2020, 63, 1245−1260

Synthesis of Compounds 2a−d. A solution of PyP4 (**1**, 200 mg, 0.33 mmol) with 1 equiv of the appropriate iodoalkane added was refluxed in glacial acetic acid (20 mL) for 76 h days under argon. The reaction mixture was concentrated *in vacuo*, and the crude compound was purified by column chromatography ($CHCl_3$/MeOH = 5:1) to afford corresponding monoalkylated derivative of PyP4. Next, a solution of appropriate intermediate and 10 equiv of iodomethane (0.20 mL, 3.23 mmol) in DMF (5 mL) under argon was stirred for 3 h at 140 °C. The DMF and excess of iodomethane were removed *in vacuo*, and the residue was dissolved in hot water and reprecipitated with acetone. The precipitated solid was filtered, washed with acetone, and dried in vacuo at RT to yield pure **2a−d**.

5-(4-*N*-Dodecylpyridyl)-10,15,20-tri(4-*N*-methylpyridyl)-21*H*,23*H*-porphyrin Tetraiodide (2a). Yield 111 mg (25%) as a purple powder, mp > 250 °C. HPLC Kromasil-100-5-mkm C-18 column (4.6 mm × 250 mm, LW = 260 nm), eluent, A, H_3PO_4 (0.01 M), B, MeCN; gradient B 25% → 60% (30 min), elution time 11.7 min, purity 98%. ^{1}H NMR (400 MHz, DMSO-d_6) δ 9.64 (d, J = 6.2 Hz, 2H, $H^{o\text{-}(N\text{-dodecyl)py}}$), 9.54 (d, J = 6.0 Hz, 6H, $H^{o\text{-}(N\text{-methyl)py}}$), 9.32 (br s, 2H, H^{pyrr}), 9.27 (br s, 6H, H^{pyrr}), 9.07−9.04 (m, 8H, $H^{m\text{-}(N\text{-alkyl)py}}$), 4.99 (t, J = 6.6 Hz, 2H, N^+CH_2), 4.77 (s, 9H, $3CH_3$), 2.37−2.29 (m, 2H, $N^+CH_2CH_2$), 1.68−1.60 (m, 2H, $CH_2^{dodecyl}$), 1.56−1.49 (m, 2H, $CH_2^{dodecyl}$), 1.46−1.28 (m, 14H, $CH_2^{dodecyl}$), 0.87 (t, J = 7.0 Hz, 3H, CH_3), −3.07 (s, 2H, 2NH). HRMS (ESI) calculated for $C_{55}H_{57}N_8$ [M − 3H]$^+$ 829.4701, found 829.4721.

5-(4-*N*-Tetradecylpyridyl)-10,15,20-tris(4-*N*-methylpyridyl)-21*H*,23*H*-porphyrin Tetraiodide (2b). Yield 113 mg (23%) as a purple powder, mp > 250 °C. HPLC Kromasil-100-5-mkm C-18 column (4.6 mm × 250 mm, LW = 260 nm), eluent, A, H_3PO_4 (0.01 M), B, MeCN; gradient B 25% → 60% (30 min), elution time 15.4 min, purity 97%. ^{1}H NMR (400 MHz, DMSO-d_6) δ 9.59 (d, J = 6.4 Hz, 2H, $H^{o\text{-}(N\text{-tetradecyl)py}}$), 9.50 (d, J = 5.9 Hz, 6H, $H^{o\text{-}(N\text{-methyl)py}}$), 9.28 (br s, 2H, H^{pyrr}), 9.23 (br s, 6H, H^{pyrr}), 9.04−9.00 (m, 8H, $H^{m\text{-}(N\text{-alkyl)py}}$), 4.96 (t, J = 6.8 Hz, 2H, N^+CH_2), 4.73 (s, 9H, $3CH_3$), 2.32−2.28 (m, 2H, $N^+CH_2CH_2$), 1.63−1.60 (m, 2H, $CH_2^{tetradecyl}$), 1.53−1.49 (m, 2H, $CH_2^{tetradecyl}$), 1.43−1.24 (m, 18H, $CH_2^{tetradecyl}$), 0.84 (t, J = 7.3 Hz, 3H, CH_3), −3.10 (s, 2H, 2NH). HRMS (ESI) calculated for $C_{57}H_{61}N_8$ [M − 3H]$^+$ 857.5014, found 857.5023.

5-(4-*N*-Hexadecylpyridyl)-10,15,20-tris(4-*N*-methylpyridyl)-21*H*,23*H*-porphyrin Tetraiodide (2c). Yield 120 mg (26%) as a purple powder, mp > 250 °C. HPLC Kromasil-100-5-mkm C-18 column (4.6 mm × 250 mm, LW = 260 nm), eluent, A, H_3PO_4 (0.01 M), B, MeCN; gradient B 25% → 60% (30 min), elution time 18.7 min, purity >99%. ^{1}H NMR (500 MHz, DMSO-d_6) δ 9.62 (d, J = 6.4 Hz, 2H, $H^{o\text{-}(N\text{-hexadecyl)py}}$), 9.52 (d, J = 6.1 Hz, 6H, $H^{o\text{-}(N\text{-methyl)py}}$), 9.30 (br s, 2H, H^{pyrr}), 9.25 (br s, 6H, H^{pyrr}), 9.06−9.02 (m, 8H, $H^{m\text{-}(N\text{-alkyl)py}}$), 4.98 (t, J = 7.3 Hz, 2H, N^+CH_2), 4.76 (s, 9H, $3CH_3$), 2.35−2.29 (m, 2H, $N^+CH_2CH_2$), 1.66−1.60 (m, 2H, $CH_2^{hexadecyl}$), 1.55−1.49 (m, 2H, $CH_2^{hexadecyl}$), 1.46−1.23 (m, 22H, $CH_2^{hexadecyl}$), 0.85 (t, J = 6.6 Hz, 3H, CH_3), −3.07 (s, 2H, 2NH). ^{13}C NMR (125 MHz, DMSO-d_6) δ 156.3 ($C^{p\text{-}(N\text{-hexadecyl)py}}$), 156.4 (3C, $C^{p\text{-}(N\text{-methyl)py}}$), 144.2 ($6C^{o\text{-}(N\text{-methyl)py}}$), 143.4 ($2C^{o\text{-}(N\text{-hexadecyl)py}}$), 132.4 ($2C^{m\text{-}(N\text{-dodecyl)py}}$), 132.0 (14C, $C^{m\text{-}(N\text{-methyl)py}}$, CH^{pyrr}), 115.8 (4C, PyrrCPyr), 60.8 (N^+CH_2), 48.0 (3C, N^+CH_3), 31.2 (CH_2CH_3), 30.9 ($N^+CH_2CH_2$), 29.0 (6C, CH_2), 28.9 (2C, CH_2), 28.6 (2C, CH_2), 25.8 (CH_2), 22.0 ($N^+CH_2CH_2CH_2$), 13.9 (CH_3). HRMS (ESI) calculated for $C_{59}H_{65}N_8$ [M − 3H]$^+$ 885.5327, found 885.5355. Elemental Analysis calculated for $C_{59}H_{68}N_8$×4I, %: C, 50.73; H, 4.91; N, 8.02. Found,%: C, 50.81; H, 4.86; N, 8.09.

5-(4-*N*-Octadecylpyridyl)-10,15,20-tris(4-*N*-methylpyridyl)-21*H*,23*H*-porphyrin Tetraiodide (2d). Yield 122 mg (26%) as a purple powder, mp > 250 °C. HPLC Kromasil-100-5-mkm C-18 column (4.6 mm × 250 mm, LW = 260 nm), eluent, A, H_3PO_4 (0.01 M), B, MeCN; gradient B 25% → 60% (30 min), elution time 22.0 min, purity 98%. ^{1}H NMR (400 MHz, DMSO-d_6) δ 9.59 (d, J = 6.5 Hz, 2H, $H^{o\text{-}(N\text{-octadecyl)py}}$), 9.51 (d, J = 6.0 Hz, 6H, $H^{o\text{-}(N\text{-methyl)py}}$), 9.29 (br s, 2H, H^{pyrr}), 9.23 (br s, 6H, H^{pyrr}), 9.04−9.01 (m, 8H, $H^{m\text{-}(N\text{-alkyl)py}}$), 4.96 (t, J = 6.5 Hz, 2H, N^+CH_2), 4.74 (s, 9H, $3CH_3$), 2.32−2.29 (m, 2H, $N^+CH_2CH_2$), 1.64−1.59 (m, 2H, $CH_2^{octadecyl}$), 1.52−1.49 (m, 2H, $CH_2^{octadecyl}$), 1.42−1.22 (m, 26H, $CH_2^{octadecyl}$), 0.84 (t, J = 6.9 Hz, 3H, CH_3), −3.10 (s, 2H, 2NH). HRMS (ESI) calculated for $C_{61}H_{69}N_8$ [M − 3H]$^+$ 913.5640, found 913.5664.

5-(4-*N*-(12-(1,3-Dioxoisoindolin-2-yl)dodecyl)pyridyl)-10,15,20-tris(4-*N*-methylpyridyl)-21*H*,23*H*-porphyrin Tetraiodide (2e). A solution of PyP4 (**1**, 400 mg, 0.66 mmol) and 2-(12-bromododecyl)isoindoline-1,3-dione (260 mg, 0.66 mmol) was refluxed in glacial acetic acid (20 mL) for 76 h under argon. After removal of acid *in vacuo*, the crude compound was purified by column chromatography (SiO_2, $CHCl_3$/MeOH = 4:1) to afford **3** (220 mg, 33%) as a purple powder, mp >250 °C. ^{1}H NMR (400 MHz, DMSO-d_6): δ = 9.56 (d, J = 6.7 Hz, 2H, $H^{o\text{-}(N\text{-dodecyl)py}}$), 9.10−9.04 (m, 10H, $H^{o\text{-}(N\text{-methyl)py}}$, H^{pyrr}), 9.01−8.99 (m, 2H, $H^{m\text{-}(N\text{-alkyl)py}}$), 8.93 (br s, 4H, H^{pyrr}), 8.28−8.27 (m, 6H, $H^{m\text{-}py}$), 7.68 (br s, 4H, H^{Pht}), 4.93 (t, J = 7.0 Hz, 2H, N^+CH_2), 3.43 (t, J = 7.0 Hz, 2H, NCH_2), 2.29−2.25 (m, 2H, $N^+CH_2CH_2$), 1.58−1.27 (m, 18H, $CH_2^{dodecyl}$), −3.09 (s, 2H, 2NH). HRMS (ESI) calculated for $C_{60}H_{54}N_9O_2$ [M]$^+$ 932.4395, found 932.4373.

A solution of the intermediate phtalimidododecyl derivative (200 mg, 0.20 mmol) and iodomethane (0.20 mL, 3.23 mmol) in DMF (5 mL) under argon was stirred for 3 h at 140 °C. The DMF and excess iodomethane were removed *in vacuo* to afford pure compound **2e** (290 mg, quantitative yield) as a purple powder, which was used without any purification, mp > 250 °C. ^{1}H NMR (400 MHz, DMSO-d_6) δ 9.55 (d, J = 6.4 Hz, 2H, $H^{o\text{-}(N\text{-dodecyl)py}}$), 9.47 (d, J = 6.1 Hz, 6H, $H^{o\text{-}(N\text{-methyl)py}}$), 9.20−9.14 (m, 8H, H^{pyrr}), 8.99−8.95 (m, 8H, $H^{m\text{-}(N\text{-alkyl)py}}$), 7.75 (br s, 4H, H^{Pht}), 4.95 (t, J = 7.0 Hz, 2H, N^+CH_2), 4.76 (s, 9H, $3CH_3$), 3.54 (t, J = 7.3 Hz, 2H, NCH_2), 2.36−2.31 (m, 2H, $N^+CH_2CH_2$), 1.68−1.27 (m, 18H, $CH_2^{dodecyl}$), −2.94 (s, 2H, 2NH). HRMS (ESI) calculated for $C_{63}H_{63}N_9O_2$ [M]$^{3+}$ 325.8361, found 325.8352.

5-(4-*N*-(12-Aminododecyl)pyridyl-10,15,20-tris(4-*N*-methylpyridyl)-21*H*,23*H*-porphyrin Pentabromide (2f). A solution of **2e** (250 mg, 0.17 mmol) in hydrobromic acid (48%, 20 mL) was refluxed for 24 h under argon. The acid was thoroughly evaporated in *in vacuo*, and the residue was reprecipitated from water with acetone to afford compound **2f** (168 mg, 80%) as a green solid, mp >250 °C. ^{1}H NMR (400 MHz, DMSO-d_6): δ = 9.64 (d, J = 6.1 Hz, 2H, $H^{o\text{-}(N\text{-dodecyl)py}}$), 9.54 (d, J = 6.1 Hz, 6H, $H^{o\text{-}(N\text{-methyl)py}}$), 9.27 (br s, 2H, H^{pyrr}), 9.21 (br s, 6H, H^{pyrr}), 9.04−9.00 (m, 8H, $H^{m\text{-}(N\text{-alkyl)py}}$), 7.79 (br s, 3H, NH_3), 4.99 (t, J = 7.3, 2H, N^+CH_2), 4.76 (s, 9H, $3CH_3$), 2.83−2.77 (m, 2H, CH_2NH_3), 2.33−2.29 (m, 2H, $N^+CH_2CH_2$), 1.63−1.33 (m, 18H, $CH_2^{dodecyl}$), −3.07 (s, 2H, 2NH). HRMS (ESI) calculated for $C_{55}H_{58}N_9$ [M − 3H]$^+$ 844.4810, found 844.4842.

5-(4-*N*-(12-*N*-Biotinylaminododecyl)pyridyl-10,15,20-tris(4-*N*-methylpyridyl)-21*H*,23*H*-porphyrin Tetrabromide (B-2a). In a solution of **2f** (125 mg, 0.10 mmol) and diisopropylethylamine (DIPEA, 0.05 mL) in DMSO (5 mL) was added a solution of biotin (31 mg, 0.11 mmol), benzotriazol-1-yloxytripyrrolidinophosphonium hexafluorophosphate (PyBOP, 55 mg, 0.11 mmol), and DIPEA (0.05 mL) in DMSO (5 mL). Reaction mixture was stirred 1 h at room temperature and diluted with an acetone−diethyl ether mixture (1:1, 20 mL), and the resulting precipitate was filtered. The residue was dissolved in a warm aqueous solution of HBr (1 N) and reprecipitated with acetone. The precipitated solid was filtered, washed with acetone, and dried *in vacuo* at RT to yield **B-2a** (95 mg, 68%) as a purple powder, mp > 250 °C. HPLC Kromasil-100-5-mkm C-18 column (4.6 mm × 250 mm, LW = 260 nm), eluent, A, H_3PO_4 (0.01 M), B, MeCN; gradient B 10% → 60% (30 min), elution time 16.9 min, purity 97%. ^{1}H NMR (500 MHz, DMSO-d_6) δ 9.63 (d, J = 6.4 Hz, 2H, $H^{o\text{-}(N\text{-dodecyl)py}}$), 9.54 (d, J = 6.4 Hz, 6H, $H^{o\text{-}(N\text{-methyl)py}}$), 9.28 (br s, 2H, H^{pyrr}), 9.22 (br s, 6H, H^{pyrr}), 9.05−9.01 (m, 8H, $H^{m\text{-}(N\text{-alkyl)py}}$), 7.81 (t, J = 5.5 Hz, NH), 6.81 (br s, 1H, NH^{biotin}), 6.43 (br s, 1H, NH^{biotin}), 4.98 (t, J = 7.0 Hz, 2H, N^+CH_2), 4.75 (s, 9H, $3CH_3$), 4.32−4.28 (m, 1H, CH_2CHNH), 4.14−4.11 (m, 1H, $CHCHNH$), 3.10−3.07 (m, 1H, SCH), 3.03−2.99 (m, 2H, CH_2NH), 2.83−2.79 (m, 1H, $SCHHCH$), 2.59−2.56 (m, 1H, $SCHHCH$), 2.33−2.29 (m, 2H, $N^+CH_2CH_2$), 2.06−2.02 (m, 2H, $COCH_2$), 1.63−1.58 (m, 2H, $N^+CH_2CH_2CH_2$), 1.52−1.47 (m, 2H, $SCHCH_2$), 1.43−1.22 (m, 20H, $10CH_2$), −3.10 (s, 2H, 2NH). ^{13}C NMR (125 MHz, DMSO-d_6) δ 171.8 (NH-C=O); 162.7 (NHCONH), 156.4 ($C^{p\text{-}(N\text{-dodecyl)py}}$), 156.2 (3C, $C^{p\text{-}(N\text{-methyl)py}}$), 144.3 (6C, $C^{o\text{-}(N\text{-methyl)py}}$), 143.4 (2C, $C^{o\text{-}(N\text{-dodecyl)py}}$), 132.5 (2C,

https://dx.doi.org/10.1021/acs.jmedchem.9b01577
J. Med. Chem. 2020, 63, 1245−1260

$C^{m\text{-}(N\text{-dodecyl)py}}$), 132.1 (14C, $C^{m\text{-}(N\text{-methyl)py}}$, CH^{pyrr}), 115.8 (4C, PyrrCPyrr), 61.1 (CHCHNH), 60.8 (N^+CH_2), 59.2 (CH_2CHNH), 55.4 (SCHCH), 47.9 (3C, N^+CH_3), 39.9 (SCH_2CH), 38.3 (CH_2NH), 35.2 (O=C−CH_2), 31.0 ($N^+CH_2CH_2$), 29.1 (CH_2), 29.0 (3C, CH_2), 28.9 (CH_2), 28.7 (CH_2), 28.6 (CH_2), 28.2 (CH_2), 28.0 (CH_2), 26.4 (CH_2), 25.8 (CH_2), 25.3 (CH_2). HRMS (ESI) calculated for $C_{65}H_{72}N_{11}O_2S$ $[M - 3H]^+$ 1070.5586, found 1070.5622. Elemental Analysis calculated for $C_{65}H_{75}N_{11}O_2S\times4Br$, %: C, 56.00; H, 5.42; N, 11.05. Found, %: 56.31, H 5.53, N 11.12.

Oligonucleotides. The oligonucleotides used in this study have been purchased from Microsynth (Switzerland). Oligonucleotide solutions (100 μM) in Milli-Q water−diethyl pyrocarbonate (DEPC) have been conserved at −80 °C. Before being used, the oligoribonucleotides in 50 mM Tris-HCl, pH 7.4, 100 mM KCl, have been heated at 90 °C for 5 min, then annealed at room temperature overnight.

Cell Culture, Metabolic Activity, and Proliferation Assays. Human pancreatic Panc-1 and MIA PaCa-2 cells, murine NIH 3T3 fibroblasts, and human embryonic kidney HEK 293 cells were maintained in exponential growth in Dulbecco's modified Eagle's medium (DMEM) containing 100 U/mL penicillin, 100 mg/mL streptomycin, 20 mM l-glutamine, and 10% fetal bovine serum (Euroclone, Italy). The metabolic activity assay was performed by seeding the cells (10×10^3 cells/well) in a 96-well plate. After 8 h, the cells have been treated with the compounds, and after an overnight incubation the cells were photoirradiated with white light (7.2 J/cm^2). Resazurin assay was performed following a standard procedure.

Stoichiometry of Binding by Continuous Variation Analysis (Job Plot). Solutions of porphyrin (TMPyP4, **2b**, and **2d**) and RG4 in 50 mM Tris-HCl, pH 7.4, and 100 mM KCl were prepared at the same concentrations of 3 μM. Two independent titrations have been carried out for each porphyrin/RG4 studied. In the first titrations, 300 μL of porphyrin solution (3 μM) was placed in the sample and reference cuvettes of the UV−vis spectrophotometer. Both solutions were titrated with RG4 (sample cuvette) and buffer (reference cuvette). In the second titration, a buffer solution containing RG4 (3 μM) was placed in the sample cuvette, while buffer was placed in the reference cuvette. Both cuvettes were titrated with porphyrin solution. The difference absorption spectra were recorded between 350 and 680 nm, and Job plots were obtained by plotting the absorbance at 424 or 447 nm against the mole fraction of porphyrin, x:

$$x = \frac{\text{moles of porphyrin}}{\text{moles of porphyrin} + \text{moles of RG4}}$$

The values of the mole fraction at maxima or minima (depending on the selected wavelength) were used to obtain the stoichiometry of porphyrin binding to RG4. UV−vis measurements have been performed on a double-bean Jasco V-750 spectrophotometer.

UV−Vis and Fluorescence Titrations. The binding of the porphyrins was determined by UV−vis titrations. A 1.6 μM solution of porphyrin in a 1 cm path length quartz cuvette was titrated with increasing aliquots of RG4. At each intermediate titration point, the fraction of bound porphyrin was calculated using the following expression:

$$f = \frac{(A_{\text{free}} - A)}{(A_{\text{free}} - A_{\text{bound}})}$$

where A_{free} and A_{bound} are the absorbance at 424 nm of free and bound porphyrin, respectively. The UV−vis measurements have been performed on a double-bean Jasco V-750 spectrophotometer.

Fluorescence titrations (1 cm cuvette) were carried on a Cary Eclipse Fluorescence Spectrophotometer. To a solution of 1.0 μM porphyrin (TMPyP4, **2b**, or **2d**) in 50 mM Tris-HCl, pH 7.4, and 100 mM KCl was added increasing amounts of RG4. After addition of RNA, the solution was mixed and equlibrated for 1 min, and a scan between 630 and 800 nm was performed at room temperature. The excitation wavelength was 420 nm. RG4 was added to the porphyrin solution until the emission was completely quenched. The fraction of bound porphyrin, f, at each intermediate titration position was calculated according to the formula:

$$f = \frac{(F_{\text{free}} - F)}{(F_{\text{free}} - F_{\text{bound}})}$$

where F_{free} and F_{bound} are the fluorescence emission of free and bound porphyrin at a selected wavelength.

Degradation of RG4 and dsRNA with Alkyl Porphyrin 2b. Solutions of 0.125 μM RG4 or double-stranded RNA labeled with Cy5.5 were incubated with yeast tRNA and 5-fold excess of porphyrin **2b** for 30 min on ice in 50 mM Tris-HCl and 100 mM KCl (RG4) or 100 mM NaCl (double-stranded RNA). The samples were photoirradiated for 0, 15, and 30 min. After that we add a stop solution and load the sample in a 20% denaturing polyacrylamide gel containing 7 M urea. Gel images were acquired on a Li-Cor imaging system (Biosciences, USA).

Western Blot Analysis. Total protein lysates (20 μg), obtained from Panc-1 cells treated with 15 nM TMPyP4, TMPyP2, **2b**, and **2d**, were electrophoresed on 12% SDS-PAGE and transferred to a nitrocellulose membrane at 100 mA for 4 h. The filter was blocked for 1 h with 5% nonfat dry milk solution in PBS 0.1% Tween (Sigma-Aldrich, Italy) at room temperature. Membranes were incubated overnight at 4 °C with primary antibodies: anti-actin (clone JLA20, IgM mouse, 1×10^{-4} μg/mL, Calbiochem, Merck Millipore, Germany), monoclonal anti-KRAS (clone 3B10-2F2, IgG_1 mouse, 2.5 μg/mL, Sigma-Aldrich, USA), monoclonal anti-NRAS (clone F155-227, IgG_1 mouse, 2.5 μg/mL, Calbiochem, Merck Millipore, Germany), monoclonal anti-PARP-1 (clone 46D11, IgG rabbit, 1:1000, Cell Signaling Technology, USA), monoclonal anti-caspase 3 (clone 3F49, IgG_{2a} mouse, 1:200, Santa Cruz Biotechnology, USA), or monoclonal anti-caspase 7 (clone 10.1.60, IgG_1 mouse, 1:200, Santa Cruz Biotechnology, USA). The filters were washed with a 5% nonfat dry milk solution in PBS 0.1% Tween and subsequently incubated for 1 h with the horseradish peroxidase conjugated secondary antibodies: anti-mouse IgG (diluted 1:5000), anti-mouse IgM (diluted 1:5000), and anti-rabbit IgG (diluted 1:5000) (Calbiochem, Merck Millipore, Germany). The signal of the proteins was developed with Super Signal West PICO and FEMTO (ThermoFisher Scientific Pierce, USA) and detected with ChemiDOC XRS, Quantity One 4.6.5 software (Bio-Rad Laboratories, USA). The exposure time depends on the antibody used and was usually between 30 s and 10 min. The protein levels were quantified by the ImageJ 1.52a (NIH, USA).

FACS Experiments: Uptake, Annexin V−PI, and ROS Detection. For uptake studies, Panc-1 cells, plated in a 12-well plate at density of 2.5×10^5 cells/well, were treated only with 5 μM CPs for 6 h or with 80 μM dynamin inhibitor I, Dynasore (Calbiochem, Merck Millipore, Germany), for 30 min and then with CPs (5 μM for 6 h). After incubation, the cells were trypsinized and pelleted. The pellets were resuspended in 500 μL of PBS and immediately analyzed by BD FACSCalibur equipped with a 488 nm argon laser. A minimum of 10^4 cells for each sample were acquired in list mode and analyzed using Cell Quest software. The cell population was analyzed by FSC light and SSC light. The signal was detected by FL3 (680 nm) channel in log scale.

Annexin V−propidium iodide assay was performed by using the Annexin-V-FLUOS Staining Kit (Roche Diagnostics GmbH, Germany) following the manufacturer instructions. Briefly, Panc-1 cells were seeded in 12-well plate (2.5×10^5 cells/well) and treated with **2b** and **2d** at different concentrations (5, 10, 15, or 20 nM). Some wells were treated also with 5 mM NAC. The day after, the plate was irradiated with white light (fluence 7.2 J/cm^2), and 6 or 24 h later, the cells were harvested by trypsinization and resuspended in Incubation buffer containing annexin-V−fluorescein and propidium iodide. After 15 min of incubation in the dark, the cells were diluted adding 200 μL of Incubation buffer and analyzed on the BD FACSCalibur flow cytometer. A minimum of 10^4 cells for each sample were acquired in list mode and analyzed using Cell Quest software. The signal was detected by FL1 (530 nm) for annexin-V and FL2 (585 nm) for propidium iodide.

https://dx.doi.org/10.1021/acs.jmedchem.9b01577
J. Med. Chem. 2020, 63, 1245−1260

For the detection of ROS by FACS, Panc-1 cells were treated with porphyrin **2b** for 16 h in the presence or absence of 5 mM NAC and then photoirradiated (fluence 7.2 J/cm^2). After 1 h, the medium was removed, the cells were washed twice with PBS and incubated with 300 μL of 10 μM CM-H$_2$DCFDA (Invitrogen, USA) in DMEM free serum for 40 min. After two washings with PBS, the cells were trypsinized and transferred into FACS tubes containing 1 mL of PBS. The suspension was centrifuged at 1200 rpm for 3 min. The pellet was suspended again in 300 μL of PBS, and the fluorescence was measured on the BD FACSCalibur flow cytometer.

RNA Extraction and Quantitative Real-Time PCR. Panc-1 cells were plated in a 96-well plate (15 × 10^3 cells/well). After 24 h, they were treated with alkyl porphyrin for 16 h in the dark, then photoirradiated (7.2 J/cm^2). Total RNA was extracted by using iScript RT-qPCR Sample Preparation Reagent (Bio-Rad Laboratories, USA) 8 h after photoirradiation. For cDNA synthesis, 1.25 μL of RNA was heated at 70 °C and placed on ice. To the solution was added 11.5 μL of a mix containin 1× buffer, 0.01 M DTT (Invitrogen, USA), 1.6 μM primer dT [MWG Biotech, Germany; d(T)$_{16}$], 1.6 μM random hexamer primers (Mycrosynth, Switzerland), 0.4 mM dNTPs solution containing equimolar amounts of dATP, dCTP, dGTP, and dTTP (Euroclone, Italy), 0.8 U/μL RNase OUT, and 8 U/μL of M-MLV reverse transcriptase (Invitrogen, USA). The mixtures were incubated for 1 h at 37 °C and stopped by heating at 95 °C for 5 min. As a negative control, the reverse transcription reaction was performed with a sample containing DEPC water. Real-time PCR multiplex reactions were performed with 1 × Kapa Probe fast qPCR kit (KAPA Biosystems, USA) for *KRAS* and housekeeping genes hypoxanthine-guanine phosphoribosyl transferase (HPRT) and β2-microglobulin and 2.2 μL of cDNA, and primers and probes are reported in Table S13, Supporting Information. The PCR cycle was 3 min at 95 °C and 50 cycles of 10 s at 95 °C, 60 s at 57.3 °C. PCR reactions were carried out with a CFX-96 real-time PCR apparatus controlled by Optical System software (version 3.1) (Bio-Rad Laboratories, USA). All expressions were normalized with housekeeping genes.

Confocal Microscopy. To determine the cellular localization of **2b** and **2d**, Panc-1 cells were plated (2.5 × 10^5 cells/dish) on coverslips placed in 35 mm Petri dishes. At 60−70% confluence, the cells were treated with 5 μM **2b** or **2d** and incubated for 6 h in the dark. Cells were then washed twice with PBS and fixed with 3% paraformaldehyde (PFA) in PBS for 20 min. After quenching with 0.1 M glycine containing 0.02% sodium azide in PBS and permeabilization with Triton X-100 (0.1% in PBS), coverslips were incubated for 5 min with Hoechst to stain the nuclei and mounted with Mowiol. Imaging was performed with a Leica TCS SP8 confocal system (Leica Microsystems GmbH, Germany) equipped with a 405 nm diode laser and a pulsed supercontinuum White Light Laser, using a 63×/1.40 oil immersion objective (Hoechst, λ_{exc} = 405 nm, detection range= 415−465 nm, PMT detector; **2b** and **2d**, λ_{exc} = 470 nm, detection range 480−749 nm, HyD detector with 0.3−6 ns time gate).

To detect intracellular ROS, Panc-1 cells were seeded (2.5 × 10^5 cells/dish) on glass-bottom 35 mm Petri dishes. The day after plating, the cells were treated overnight with the cationic porphyrins at the concentration of 15 nM, followed by 1 h incubation with the ROS-sensitive fluorescent indicator CM-H$_2$DCFDA (10 μM) in the absence and presence of 5 mM NAC. The control samples were not treated with porphyrins. Then the plates were irradiated with white light (fluence 7.2 J/cm^2), and the ROS levels were detected by confocal microscopy after 1 h from irradiation. Live differential interference contrast (DIC) and confocal images were acquired on a Leica TCS SP8 confocal system equipped with a 63×/1.40 oil immersion objective and White Light Laser (CM-H$_2$DCFDA, λ_{exc}= 495 nm, detection range 505−575 nm, PMT detector). Fluorescence was quantified from five representative fields per condition using LAS X version 3.5.5 software (Leica Microsystem GmbH, Germany).

Biotin−Streptavidin Pull-Down Experiments. *Calibration Plot.* To construct the calibration plot for biotin−streptavidin pull down assays, we prepared several mixtures of 95- and 89-nt sequences in 50 mM Tris-HCl, pH 7.4, 50 mM KCl, at total concentration of 0.2 μM and 95-nt/89-nt ratio varying from 0.25 to 2. The mixtures have been amplified with KAPA2G Robust HotStart PCR Kit (KAPA Biosystems, USA) using the same couple of primers (sequences reported in Table S13, Supporting Information) (0.5 μM) and dNTPs (0.2 mM). The program was 5 min 95 °C, 15 s 95 °C, 15 s 55 °C, 30 s 72 °C, 35 cycles. The products have been separated by 12% PAGE, and the bands were stained with stain all. Their intensities were measured with a ChemiDOC XRS, Quantity One 4.6.5 software (Bio-Rad Laboratories, USA).

Pull-Down with Cellular RNA. Total RNA was extracted from Panc-1 cells with TRIZOL (Invitrogene, USA) and its concentration was measured by UV absorption. Eight micrograms of cellular RNA in 50 mM KCl, 50 mM Tris-HCl, pH 7.4, was incubated overnight with increasing concentrations of ligand **B-2a** (from 0.2 to 0.6 μM, 4 °C). We incubated the magnetic beads, after saturation with tRNA, with cellular RNA treated with the biotinylated ligand for 30 min at 25 °C. The supernatant was removed, and the beads were washed three times with 50 mM Tris-HCl, pH 7.4, 50 mM KCl. We then recovered the bound RNA with a solution of 0.8 M NaCl. The recovered RNA was retrotranscribed with 0.8 U/μL RNase OUT and 8 U/μL of M-MLV reverse transcriptase (Life Technologies, Thermo Fisher, USA) and amplified by quantitative real-time PCR (vide infra). We amplified *KRAS* and the housekeeping gene HPRT (primers in Table S13, Supporting Information).

Antitumor Activity in SCID Mice. Female SCID mice were obtained from Harlan-Nossan (Italy) and maintained in a conventional animal house for 2 weeks. All procedures with animals were carried out in accordance with the National Institutional Animal Care Committee at the University of Trieste and the ACS Ethical Guidelines. Every effort was made to avoid unnecessary pain to the animals. Into the upper flank of mice (weighing ∼20 g), 15 × 10^6 Panc-1 cells harvested from a cell culture were implanted by subcutaneous injection. After 2 weeks, the tumors reached a size of 6−8 mm (along the largest diameter), and the mice were randomized into groups of 3−4 mice each (18 total mice), and the porphyrins (TMPyP2, 30 mg/kg; **2b**, 3 mg/kg) were injected into the tumors. About 2 h after injection, the mice were anesthetized with zoletil + xylazine (15 mg/kg + 5 mg/kg; ip), shaved in the tumor area, and irradiated with a laser BWN-660-60E [B&WTEK, Inc., Newark, DE, USA] at 660 ± 5 nm, at fluence of 193 J/cm^2. The mice were examined every 2 days for changes in weight, appearance of side effects, or signs of sickness. The size of the tumor was measured every 2−3 days with a micrometer caliper. The mass (mg) of the tumor was calculated assuming a tumor density of 1 and a tumor volume given by $(\pi/6)a^2b$ where a and b are the shorter and larger axes (mm), respectively.

Statistical Analysis. Data are reported as mean values ± standard error (SE). Statistical analyses were carried out using Sigma Plot software. Group differences were analyzed by Student's t-test or one-way analysis of variance (ANOVA). Groups are considered different when $P < 0.05$.

■ ASSOCIATED CONTENT

Supporting Information

The Supporting Information is available free of charge at https://pubs.acs.org/doi/10.1021/acs.jmedchem.9b01577.

Synthesis of biotinylated **B-2a**, ^{1}H and ^{13}C NMR spectra, UV spectra, and HPLC of porphyrins **2a−d**, 5′-UTR of NRAS, CD and melting, Job plots, SPR sensorgrams, alkyl porphyrin uptake at 4 and 37 °C, metabolic activity of MIA PaCa-2 and HEK 293 cells, effect of porphyrin on metabolic activity in the dark, list of DNA primers (PDF)

Molecular formula strings for all the final target compounds (CSV)

■ AUTHOR INFORMATION

Corresponding Author

Luigi E. Xodo − *Department of Medicine, Laboratory of Biochemistry, Univeristy of Udine, Udine 33100, Italy;*

https://dx.doi.org/10.1021/acs.jmedchem.9b01577
J. Med. Chem. 2020, 63, 1245−1260

orcid.org/0000-0003-3344-7207; Email: luigi.xodo@uniud.it

Authors

Annalisa Ferino − *Department of Medicine, Laboratory of Biochemistry, Univeristy of Udine, Udine 33100, Italy*
Giulia Nicoletto − *Department of Medicine, Laboratory of Biochemistry, Univeristy of Udine, Udine 33100, Italy*
Francesca D'Este − *Department of Medicine, Laboratory of Biochemistry, Univeristy of Udine, Udine 33100, Italy*
Sonia Zorzet − *Department of Life Science, University of Trieste, Trieste 34127, Italy*
Sara Lago − *Department of Molecular Medicine, University of Padova, Padova 35121, Italy*
Sara N. Richter − *Department of Molecular Medicine, University of Padova, Padova 35121, Italy;* orcid.org/0000-0002-5446-9029
Alexander Tikhomirov − *Gause Institute of New Antibiotics, Moscow 119021, Russia*
Andrey Shchekotikhin − *Gause Institute of New Antibiotics, Moscow 119021, Russia*

Complete contact information is available at: https://pubs.acs.org/10.1021/acs.jmedchem.9b01577

Author Contributions

[⊥]A.F. and G.N. contributed equally. L.E.X. and A.S. designed the research; L.E.X., A.S., S.Z., and S.N.R. designed the experiments; A.F., G.N., F.D., S.L., S.Z., and A.T. carried out the experiments; L.E.X. wrote the article with the contributions of A.F., A.S., and S.N.R.

Notes

The authors declare no competing financial interest.

■ ACKNOWLEDGMENTS

This study has been carried out with the financial support of AIRC (Italian Association for Cancer Research) Grant IG-2017, Project Code 19898 (Luigi Xodo).

■ ABBREVIATIONS

KRAS, Kirsten ras; *NRAS*, neuroblastoma ras; *HPRT*, hypoxanthine phosphoribosyl tranferase; SCID, severe combined immunodeficient; CD, circular dichroism; RG4, RNA G-quadruplex; SPR, surface plasmon resonance; PDT, photodynamic therapy; CP, cationic porphyrin; PDAC, pancreatic ductal adenocarcinoma; DMSO, dimethyl sulfoxide; DMF, dimethylformamide; NAC, *N*-acetylcysteine; PI, propidium iodide; CM-H_2DCFDA, chloromethyl-2′,7′-dichlorodihydrofluorescein diacetate; HEK 293, human embryonic kidney 293 cells; NIH 3T3, mouse embryo fibroblast cells

■ REFERENCES

(1) Hobbs, A. G.; Der, C. J.; Rossman, K. L. RAS isoforms and mutations in cancer at a glance. *J. Cell Sci.* **2016**, *129*, 1287−1292.
(2) Prior, I. A.; Lewis, P. D.; Mattos, C. A comprehensive survey of ras mutations in cancer. *Cancer Res.* **2012**, *72*, 2457−2467.
(3) Hruban, R. H.; Goggins, M.; Parsons, J.; Kern, S. E. Progression model for pancreatic cancer. *Clin. Cancer Res.* **2000**, *6*, 2969−2972.
(4) Hingorani, S. R.; Petricoin, E. F.; Maitra, A.; Rajapakse, V.; King, C.; Jacobetz, M. A.; Ross, S.; Conrads, T. P.; Veenstra, T. D.; Hitt, B. A.; Kawaguchi, Y.; Johann, D.; Liotta, L. A.; Crawford, H. C.; Putt, M. E.; Jacks, T.; Wright, C. V.; Hruban, R. H.; Lowy, A. M.; Tuveson, D. A. Preinvasive and invasive ductal pancreatic cancer and its early detection in the mouse. *Cancer Cell* **2003**, *4*, 437−450.
(5) Hingorani, S. R.; Wang, L.; Multani, A. S.; Combs, C.; Deramaudt, T. B.; Hruban, R. H.; Rustgi, A. K.; Chang, S.; Tuveson, D. A. Trp53R172H and KrasG12D cooperate to promote chromosomal instability and widely metastatic pancreatic ductal adenocarcinoma in mice. *Cancer Cell* **2005**, *7*, 469−483.
(6) Bardeesy, N.; Aguirre, A. J.; Chu, G. C.; Cheng, K. H.; Lopez, L. V.; Hezel, A. F.; Feng, B.; Brennan, C.; Weissleder, R.; Mahmood, U.; Hanahan, D.; Redston, M. S.; Chin, L.; DePinho, R. A. Both p16Ink4a and the p19Arf-p53 pathway constrain progression of pancreatic adenocarcinoma in the mouse. *Proc. Natl. Acad. Sci. U. S. A.* **2006**, *103*, 5947−5952.
(7) Waters, A. M.; Der, C. J. KRAS: The Critical driver and therapeutic target for pancreatic cancer. *Cold Spring Harbor Perspect. Med.* **2018**, *8*, No. a031435.
(8) McCormick, F. Cancer therapy based on oncogene addiction. *J. Surg. Oncol.* **2011**, *103*, 464−467.
(9) Ying, H.; Kimmelman, A. C.; Lyssiotis, C. A.; Hua, S.; Chu, G. C.; Fletcher-Sananikone, E.; Locasale, J. W.; Son, J.; Zhang, H.; Coloff, J. L.; Yan, H.; Wang, W.; Chen, S.; Viale, A.; Zheng, H.; Paik, J. H.; Lim, C.; Guimaraes, A. R.; Martin, E. S.; Chang, J.; Hezel, A. F.; Perry, S. R.; Hu, J.; Gan, B.; Xiao, Y.; Asara, J. M.; Weissleder, R.; Wang, Y. A.; Chin, L.; Cantley, L. C.; DePinho, R. A. Oncogenic KRAS maintains pancreatic tumors through regulation of anabolic glucose metabolism. *Cell* **2012**, *149*, 656−670.
(10) Weinstein, I. B.; Joe, A.; Felsher, D. Oncogene addiction. *Cancer Res.* **2008**, *68*, 3077−3080.
(11) Spiegel, J.; Cromm, P. M.; Zimmermann, G.; Grossmann, T. N.; Waldmann, H. Small-molecule modulation of ras signaling. *Nat. Chem. Biol.* **2014**, *10*, 613−622.
(12) Michalski, C. W.; Hackert, T.; Buchler, M. W. Targeting metabolism in pancreatic cancer. *Lancet Oncol.* **2017**, *18*, 699−700.
(13) Kawada, K.; Toda, K.; Sakai, Y. Targeting metabolic reprogramming in KRAS-driven cancers. *Int. J. Clin. Oncol.* **2017**, *22*, 651−659.
(14) Cohen, R.; Neuzillet, C.; Tijeras-Raballand, A.; Faivre, S.; de Gramont, A.; Raymond, E. Targeting cancer cell metabolism in pancreatic adenocarcinoma. *Oncotarget* **2015**, *6*, 16832−16847.
(15) McCormick, F. KRAS as a therapeutic target. *Clin. Cancer Res.* **2015**, *21*, 1797−1801.
(16) Dang, C. V.; Reddy, E. P.; Shokat, K. M.; Soucek, L. Drugging the 'undruggable' cancer targets. *Nat. Rev. Cancer* **2017**, *17*, 502−508.
(17) McCormick, F. Targeting KRAS directly. *Annual Review of Cancer Biology* **2018**, *2*, 81−90.
(18) Miglietta, G.; Cogoi, S.; Marinello, J.; Capranico, G.; Tikhomirov, A. S.; Shchekotikhin, A.; Xodo, L. E. RNA G-quadruplexes in Kirsten ras (KRAS) oncogene as targets for small molecules inhibiting translation. *J. Med. Chem.* **2017**, *60*, 9448−9461.
(19) Wheelhouse, R. T.; Sun, D.; Han, H.; Han, F. X.; Hurley, L. H. Cationic porphyrins as telomerase inhibitors: the interaction of tetra-(N-methyl-4-pyridyl)porphine with quadruplex DNA. *J. Am. Chem. Soc.* **1998**, *120*, 3261−3262.
(20) Zamiri, B.; Reddy, K.; Macgregor, R. B., Jr; Pearson, C. E. TMPyP4 porphyrin distorts RNA G-quadruplex structures of the disease-associated r(GGGGCC)n repeat of the C9orf72 gene and blocks interaction of RNA-binding proteins. *J. Biol. Chem.* **2014**, *289*, 4653−4659.
(21) Xodo, L. E.; Cogoi, S.; Rapozzi, V. Photosensitizers binding to nucleic acids as anticancer agents. *Future Med. Chem.* **2016**, *8*, 179−194.
(22) Bhattacharyya, D.; Arachchilage, G. M.; Basu, S. Metal cations in G-quadruplex folding and stability. *Front. Chem.* **2016**, *4*, No. 38.
(23) Cogoi, S.; Xodo, L. E. G4 DNA in ras genes and its potential in cancer therapy. *Biochim. Biophys. Acta, Gene Regul. Mech.* **2016**, *1859*, 663−674.
(24) Balasubramanian, S.; Hurley, L. H.; Neidle, S. Targeting G-quadruplexes in gene promoters: a novel anticancer strategy? *Nat. Rev. Drug Discovery* **2011**, *10*, 261−275.
(25) Siddiqui-Jain, A.; Grand, C. L.; Bearss, D. J.; Hurley, L. H. Direct evidence for a G-quadruplex in a promoter region and its targeting with

a small molecule to repress c-MYC transcription. *Proc. Natl. Acad. Sci. U. S. A.* **2002**, *99*, 11593−11598.
(26) Song, J.; Perreault, J. P.; Topisirovic, I.; Richard, S. RNA G-quadruplexes and their potential regulatory roles in translation. *Translation (Austin)* **2016**, *4*, No. e1244031.
(27) Bugaut, A.; Balasubramanian, S. 5′-UTR RNA G-quadruplexes: translation regulation and targeting. *Nucleic Acids Res.* **2012**, *40*, 4727−4741.
(28) Ricchelli, F.; Franchi, L.; Miotto, G.; Borsetto, L.; Gobbo, S.; Nikolov, P.; Bommer, J. C.; Reddi, E. Meso-substituted tetra-cationic porphyrins photosensitize the death of human fibrosarcoma cells via lysosomal targeting. *Int. J. Biochem. Cell Biol.* **2005**, *37*, 306−319.
(29) Villanueva, A.; Jori, G. Pharmacokinetic and tumor-photosensitizing properties of the cationic porphyrin meso-tetra(4N-methylpyridyl)porphine. *Cancer Lett.* **1993**, *73*, 59−64.
(30) Rapozzi, V.; Zorzet, S.; Zacchigna, M.; Della Pietra, E.; Cogoi, S.; Xodo, L. E. Anticancer activity of cationic porphyrins in melanoma tumor-bearing mice and mechanistic in vitro studies. *Mol. Cancer* **2014**, *13*, 75−87.
(31) Cogoi, S.; Zorzet, S.; Rapozzi, V.; Géci, I.; Pedersen, E. B.; Xodo, L. E. MAZ-binding G4-decoy with locked nucleic acid and twisted intercalating nucleic acid modifications suppresses KRAS in pancreatic cancer cells and delays tumor growth in mice. *Nucleic Acids Res.* **2013**, *41*, 4049−4064.
(32) Stallivieri, A.; Le Guern, F.; Vanderesse, R.; Meledje, E.; Jori, G.; Frochot, C.; Acherar, S. Synthesis and photophysical properties of the photoactivatable cationic porphyrin 5-(4-N-dodecylpyridyl)-10,15,20-tri(4-N-methylpyridyl)-21H,23H-porphyrin tetraiodide for anti-malaria PDT. *Photochem. Photobiol. Sci.* **2015**, *14*, 1290−1295.
(33) Goff, H. M.; Morgan, L. O. Carbon-13 and proton nuclear magnetic resonance spectroscopy of water-soluble porphyrins and metalloporphyrins. *Bioinorg. Chem.* **1978**, *9*, 61−79.
(34) Sabharwal, N. C.; Mendoza, O.; Nicoludis, J. M.; Ruan, T.; Mergny, J. L.; Yatsunyk, L. A. Investigation of the interactions between Pt(II) and Pd(II) derivatives of 5,10,15,20-tetrakis (N-methyl-4-pyridyl) porphyrin and G-quadruplex DNA. *JBIC, J. Biol. Inorg. Chem.* **2016**, *21*, 227−239.
(35) Boschi, E.; Davis, S.; Taylor, S.; Butterworth, A.; Chirayath, L. A.; Purohit, V.; Siegel, L. K.; Buenaventura, J.; Sheriff, A. H.; Jin, R.; Sheardy, R.; Yatsunyk, L. A.; Azam, M. Interaction of a cationic porphyrin and its metal derivatives with G□quadruplex DNA. *J. Phys. Chem. B* **2016**, *120*, 12807−12819.
(36) Wang, K.; You, M.; Chen, Y.; Han, D.; Zhu, Z.; Huang, J.; Williams, K.; Yang, C. J.; Tan, W. Self-assembly of a bifunctional DNA carrier for drug delivery. *Angew. Chem., Int. Ed.* **2011**, *50*, 6098−6101.
(37) Zhang, H. J.; Wang, X. F.; Wang, P.; Ai, X. C.; Zhang, J. P. Spectroscopic study on the binding of a cationic porphyrin to DNA G-quadruplex under different K+ concentrations. *Photochem. Photobiol. Sci.* **2008**, *7*, 948−955.
(38) Sazanovich, I. V.; Petrov, E. P.; Chirvony, V. S. Interaction of cationic porphyrin 5,10,1520- tetrakis (4-N-methylpyridyl)porphyrin with mono and polynucleotides: a study by picosecond fluorescence. *Opt. Spectrosc.* **2006**, *100*, 209−218.
(39) Grand, C. L.; Han, H.; Muñoz, R. M.; Weitman, S.; Von Hoff, D. D.; Hurley, L. H.; Bearss, D. J. The cationic porphyrin TMPyP4 down-regulates c-MYC and human telomerase reverse transcriptase expression and inhibits tumor growth in vivo. *Mol. Cancer Ther.* **2002**, *1*, 565−573.
(40) Ren, J.; Chaires, J. B. Sequence and structural selectivity of nucleic acid binding ligands. *Biochemistry* **1999**, *38*, 16067−16075.
(41) Sever, S. Dynamin and endocytosis. *Curr. Opin. Cell Biol.* **2002**, *14*, 463−467.
(42) Bugaut, A.; Alberti, P. Understanding the stability of DNA G-quadruplex units in long human telomeric strands. *Biochimie* **2015**, *113*, 125−133.
(43) Wu, D.; Yotnda, P. Production and detection of reactive oxygen species (ROS) in cancers. *J. Visualized Exp.* **2011**, *57*, No. e3357.
(44) Zafarullah, M.; Li, W. Q.; Sylvester, J.; Ahmad, M. Molecular mechanisms of N-acetylcysteine actions. *Cell. Mol. Life Sci.* **2003**, *60*, 6−20.
(45) Endoh, T.; Sugimoto, N. Mechanical insights into ribosomal progression overcoming RNA G-quadruplex from periodical translation suppression in cells. *Sci. Rep.* **2016**, *6*, 22719.
(46) Beaudoin, J. D.; Perreault, J. P. 5′-UTR G-quadruplex structures acting as translational repressors. *Nucleic Acids Res.* **2010**, *38*, 7022−7036.
(47) Chaitanya, G. V.; Alexander, J. S.; Babu, P. P. PARP-1 cleavage fragments: signatures of cell-death proteases in neurodegeneration. *Cell Commun. Signaling* **2010**, *8*, 31−42.
(48) DeNicola, G. M.; Karreth, F. A.; Humpton, T. J.; Gopinathan, A.; Wei, C.; Frese, K.; Mangal, D.; Yu, K. H.; Yeo, C. J.; Calhoun, E. S.; Scrimieri, F.; Winter, J. M.; Hruban, R. H.; Iacobuzio-Donahue, C.; Kern, S. E.; Blair, I. A.; Tuveson, D. A. Oncogene-induced Nrf2 transcription promotes ROS detoxification and tumorigenesis. *Nature* **2011**, *475*, 106−109.
(49) Ferino, A.; Rapozzi, V.; Xodo, L. E. The ROS-KRAS-Nrf2 axis in the control of the redox homeostasis and its intersection with survival-apoptosis pathways. *J. Photochem. Photobiol., B* **2020**, *202*, 111672.
(50) Lister, A.; Nedjadi, T.; Kitteringham, N. R.; Campbell, F.; Costello, E.; Lloyd, B.; Copple, I. M.; Williams, S.; Owen, A.; Neoptolemos, J. P.; Goldring, C. E.; Park, B. K. Nrf2 is overexpressed in pancreatic cancer: implications for cell proliferation and therapy. *Mol. Cancer* **2011**, *10*, 37−50.
(51) Hong, Y. B.; Kang, H. J.; Kwon, S. Y.; Kim, H. J.; Kwon, K. Y.; Cho, C. H.; Lee, J. M.; Kallakury, B. V.; Bae, I. Nuclear factor (erythroid-derived 2)-like 2 regulates drug resistance in pancreatic cancer cells. *Pancreas* **2010**, *39*, 463−472.
(52) Burris, H. A., 3rd; Moore, M. J.; Andersen, J.; Green, M. R.; Rothenberg, M. L.; Modiano, M. R.; Cripps, M. C.; Portenoy, R. K.; Storniolo, A. M.; Tarassoff, P.; Nelson, R.; Dorr, F. A.; Stephens, C. D.; Von Hoff, D. D. Improvements in survival and clinical benefit with gemcitabine as first-line therapy for patients with advanced pancreas cancer: a randomized trial. *J. Clin. Oncol.* **1997**, *15*, 2403−2413.
(53) Kawauchi, K.; Sugimoto, W.; Yasui, T.; Murata, K.; Itoh, K.; Takagi, K.; Tsuruoka, T.; Akamatsu, K.; Tateishi-Karimata, H.; Sugimoto, N.; Miyoshi, D. An anionic phthalocyanine decreases NRAS expression by breaking down its RNA G-quadruplex. *Nat. Commun.* **2018**, *9*, 2271.

https://dx.doi.org/10.1021/acs.jmedchem.9b01577
J. Med. Chem. 2020, 63, 1245−1260